

## THE KMOS<sup>3D</sup> SURVEY: DESIGN, FIRST RESULTS, AND THE EVOLUTION OF GALAXY KINEMATICS FROM $0.7 \leq z \leq 2.7$ \*

E. WISNOSKI<sup>1</sup>, N. M. FÖRSTER SCHREIBER<sup>1</sup>, S. WUYTS<sup>1</sup>, E. WUYTS<sup>1</sup>, K. BANDARA<sup>1</sup>, D. WILMAN<sup>2,1</sup>, R. GENZEL<sup>1,3,4</sup>,  
R. BENDER<sup>1,2</sup>, R. DAVIES<sup>1</sup>, M. FOSSATI<sup>2,1</sup>, P. LANG<sup>1</sup>, J. T. MENDEL<sup>1</sup>, A. BEIFIORI<sup>1,2</sup>, G. BRAMMER<sup>5</sup>, J. CHAN<sup>1</sup>, M. FABRICIUS<sup>1</sup>,  
Y. FUDAMOTO<sup>1</sup>, S. KULKARNI<sup>1</sup>, J. KURK<sup>1</sup>, D. LUTZ<sup>1</sup>, E. J. NELSON<sup>6</sup>, I. MOMCHEVA<sup>6</sup>, D. ROSARIO<sup>1</sup>, R. SAGLIA<sup>1</sup>, S. SEITZ<sup>1,2</sup>,  
L. J. TACCONI<sup>1</sup>, AND P. G. VAN DOKKUM<sup>6</sup>

<sup>1</sup> Max-Planck-Institut für extraterrestrische Physik (MPE), Giessenbachstr. 1, D-85748 Garching, Germany;  
[emily@mpe.mpg.de](mailto:emily@mpe.mpg.de)

<sup>2</sup> Universitäts-Sternwarte, Ludwig-Maximilians-Universität, Scheinerstrasse 1, D-81679 München, Germany

<sup>3</sup> Department of Physics, Le Conte Hall, University of California, Berkeley, CA 94720, USA

<sup>4</sup> Department of Astronomy, Hearst Field Annex, University of California, Berkeley, CA 94720, USA

<sup>5</sup> Space Telescope Science Institute, 3700 San Martin Drive, Baltimore, MD 21218, USA

<sup>6</sup> Department of Astronomy, Yale University, New Haven, CT 06511, USA

*Received 2014 September 22; accepted 2014 November 25; published 2015 January 30*

### ABSTRACT

We present the KMOS<sup>3D</sup> survey, a new integral field survey of over 600 galaxies at  $0.7 < z < 2.7$  using KMOS at the Very Large Telescope. The KMOS<sup>3D</sup> survey utilizes synergies with multi-wavelength ground- and space-based surveys to trace the evolution of spatially resolved kinematics and star formation from a homogeneous sample over 5 Gyr of cosmic history. Targets, drawn from a mass-selected parent sample from the 3D-HST survey, cover the star formation–stellar mass ( $M_*$ ) and rest-frame  $(U - V) - M_*$  planes uniformly. We describe the selection of targets, the observations, and the data reduction. In the first-year of data we detect H $\alpha$  emission in 191  $M_* = 3 \times 10^9 - 7 \times 10^{11} M_\odot$  galaxies at  $z = 0.7-1.1$  and  $z = 1.9-2.7$ . In the current sample 83% of the resolved galaxies are rotation dominated, determined from a continuous velocity gradient and  $v_{\text{rot}}/\sigma_0 > 1$ , implying that the star-forming “main sequence” is primarily composed of rotating galaxies at both redshift regimes. When considering additional stricter criteria, the H $\alpha$  kinematic maps indicate that at least  $\sim 70\%$  of the resolved galaxies are disk-like systems. Our high-quality KMOS data confirm the elevated velocity dispersions reported in previous integral field spectroscopy studies at  $z \gtrsim 0.7$ . For rotation-dominated disks, the average intrinsic velocity dispersion decreases by a factor of two from  $50 \text{ km s}^{-1}$  at  $z \sim 2.3$  to  $25 \text{ km s}^{-1}$  at  $z \sim 0.9$ . Combined with existing results spanning  $z \sim 0-3$ , we show that disk velocity dispersions follow an evolution that is consistent with the dependence of velocity dispersion on gas fractions predicted by marginally stable disk theory.

*Key words:* galaxies: evolution – galaxies: high-redshift – galaxies: kinematics and dynamics – infrared: galaxies

### 1. INTRODUCTION

The baryonic growth of galaxies near the peak of the galaxy formation epoch was dominated by in situ star formation maintained through an equilibrium of gas accretion from the cosmic web and (mainly) minor mergers, with star formation and gas recycling through the circumgalactic medium driven by stellar and active galactic nucleus (AGN) feedback (e.g., Bower et al. 2006; Dekel et al. 2009; Bouché et al. 2010; Dutton et al. 2010; Guo et al. 2010; Davé et al. 2012; Lilly et al. 2013; Vogelsberger et al. 2013; Dekel & Mandelker 2014; Schaye et al. 2015; Sparre et al. 2014). The balance between these mechanisms maintains galaxies on a tight “main sequence” (MS) in star formation rate (SFR) versus stellar mass ( $M_*$ ), with  $\sim 0.3$  dex scatter. The decreasing zero point of the MS reflects the evolution of the cosmic SFR density from the “peak activity” at  $z \sim 1-2.5$  to the “winding down” epochs at  $z < 1$  (e.g., Noeske et al. 2007; Daddi et al. 2007b; Elbaz et al. 2007; Rodighiero et al. 2011; Whitaker et al. 2014). This scenario is further empirically motivated by the dominance of disk-like systems among MS star-forming galaxies (SFGs) out to  $z \sim 2.5$  (e.g., Förster Schreiber et al. 2006, 2009; Genzel et al. 2006, 2008; Shapiro et al. 2008; Epinat et al. 2009, 2012; Wuyts et al.

2011b) and the evolution of molecular gas mass fractions (e.g., Tacconi et al. 2010, 2013; Daddi et al. 2010; Saintonge et al. 2013; Genzel et al. 2014c).

In this picture, galaxies grow in stellar mass mostly while on the MS (e.g., Rodighiero et al. 2011). Rare occasional bursts of star formation can lead to temporary offsets above the MS (e.g., through mergers). Above  $M_* \sim 10^{11} M_\odot$ , most galaxies appear to be rapidly quenched dropping below the MS at  $z \lesssim 2.5$  (Peng et al. 2010; Whitaker et al. 2012a). Spatially resolved information of the kinematics, star formation and nebular conditions provide key insights into the processes that drive galaxy growth, bursts, and quenching by probing their dynamical state and key signatures of secular- or merger-driven growth.

Resolved kinematic surveys that utilize integral field spectroscopy (IFS)—ranging from a handful to  $\sim 100$  SFGs—have been critical in establishing this picture. By revealing the kinematic nature and prevalence of rotating disks among luminous SFGs at  $z \sim 1-4$ , these surveys have contributed key evidence in support of “smoother” mass accretion and for the importance of internal dynamical processes in the early evolution of massive galaxies (e.g., Genzel et al. 2006, 2008; Förster Schreiber et al. 2006; Wright et al. 2009; Law et al. 2009; Förster Schreiber et al. 2009; Epinat et al. 2009, 2012; Wisnioski et al. 2011; Contini et al. 2012; Swinbank et al. 2012; Sobral et al. 2013; Stott et al. 2014). However, due to practical

\* Based on observations obtained at the Very Large Telescope (VLT) of the European Southern Observatory (ESO), Paranal, Chile (ESO program IDS 092A-0091, 093.A-0079).

limitations of sample selection and telescope time, large statistical and cohesive data sets at  $z \gtrsim 1$  have been unattainable especially at the depth required to measure subtle kinematic and emission line features (see Glazebrook 2013 for a review of IFS results). Currently, a new multiplexed generation has begun for high-redshift galaxy studies of dynamics and chemical evolution with the advent of deployable integral field unit (IFU) systems and multi-object spectrographs operating in the near-infrared where key emission lines are redshifted at  $0.5 \lesssim z \lesssim 3$ .

In this paper we introduce the KMOS<sup>3D</sup> Survey—hereafter simply KMOS<sup>3D</sup>—a survey that leverages new rest-frame-optical redshift catalogs with the multiplex of a deployable IFU system for a 20-fold increase in efficiency over previous single-IFU surveys. KMOS<sup>3D</sup> is a guaranteed time program using the K-band Multi-Object Spectrograph (KMOS; Sharples et al. 2004, 2013) on the Very Large Telescope (VLT) to map kinematics, star formation, metallicity and the physical conditions of the ISM of a mass-selected sample. Primary emission lines of interest are  $H\alpha$ , [NII], and [SII], observed through the  $YJ$ ,  $H$ , and  $K$  atmospheric windows probing galaxies at  $0.7 < z < 2.7$ .

Our strategy is designed to achieve a wide and uniform coverage of the SFG population at  $M_* \gtrsim 10^{9.5} M_\odot$  while still obtaining high signal-to-noise ratio (S/N) data of individual galaxies to determine good-quality line ratios and line profiles in individual galaxies. The baseline sample is 600 galaxies—balancing observational depth with the statistics required to explore trends of kinematic properties as a function of, e.g.,  $M_*$ , SFR,  $(U - V)_{\text{rest}}$  color, and redshift with 10–20 galaxies in individual  $M_*$ , SFR,  $(U - V)_{\text{rest}}$  bins. KMOS<sup>3D</sup> targets are drawn from the 3D-HST space-based near-infrared (IR) grism survey (Brammer et al. 2012; Skelton et al. 2014). The 3D-HST sample, with grism- and spectroscopic-based redshifts, forms a more representative sample of the full SFG population (including dusty and low sSFR galaxies) than rest-UV spectroscopic samples, from which many past IFS targets were drawn.

Capitalizing on crucial synergies with multi-wavelength ground- and space-based surveys, KMOS<sup>3D</sup> will draw connections between ionized gas properties (spatially resolved kinematics, star formation, outflows, excitation and metallicity) and stellar properties (stellar structure, stellar populations, and environment) to provide constraints on the physical mechanisms driving mass growth, feedback, and star formation shutdown. These connections have already been proved possible with the first-year data from KMOS<sup>3D</sup>, which reveal nuclear outflows in a high fraction of  $\log(M_* [M_\odot]) > 10.9$  galaxies (Genzel et al. 2014b) and confirm an evolution to lower [NII]/ $H\alpha$  at earlier times but find no correlation between [NII]/ $H\alpha$  and SFR (Wuyts et al. 2014).

This paper focuses on the kinematic properties derived from  $H\alpha$ , near-IR continuum, velocity, and velocity dispersion maps. We combine galaxy dynamics, structural parameters, and multi-band imaging to make robust kinematic determinations for  $>100$  galaxies between  $0.7 < z < 2.7$ , expanding the redshift range of previous individual surveys with homogeneous selection and ancillary data. The wide redshift range and large data set of the full sample will consistently track the evolution of galaxies from the peak in cosmic SFR density into the epochs of its decline.

Previous IFS and long-slit observations of high-redshift SFGs have revealed large ionized gas velocity dispersions—5–10 $\times$  local galaxies—after correcting for instrumental resolution and rotational broadening (e.g., Weiner et al. 2006; Förster Schreiber

et al. 2006, 2009; Genzel et al. 2006; Law et al. 2007, 2009; Wright et al. 2009; Gnerucci et al. 2011; Wisnioski et al. 2011; Epinat et al. 2012; Swinbank et al. 2012; Kassin et al. 2012). Various origins have been proposed for the high velocity dispersions such as feedback (Dib et al. 2006; Green et al. 2010), gas accretion (Förster Schreiber et al. 2006; Genzel et al. 2006; Elmegreen & Burkert 2010; Genel et al. 2010; Forbes et al. 2012), conversion of gravitational potential energy into random motions either at the outer disk/cosmic web boundary (Förster Schreiber et al. 2006; Genzel et al. 2006, 2008; Cacciato et al. 2012) or in the inner disk by torques in clump–clump interactions (Immeli et al. 2004; Bournaud et al. 2010; Aumer et al. 2010). We exploit here our first-year results to set tighter constraints on the evolution and origin of disk velocity dispersions.

This paper is organized as follows. Section 2 describes the KMOS<sup>3D</sup> sample selection, first-year observations, and data reduction. Section 3 describes the  $H\alpha$ -detected galaxies and presents their kinematic maps and the methods used to derive their kinematic properties, which are used in Section 4 to determine galaxy classifications. In Section 5 we utilize the new KMOS<sup>3D</sup> results at  $z \sim 1$  and  $z \sim 2$  to investigate the evolution of disk velocity dispersion of ionized gas and possible dependencies on other derived properties. This paper is summarized in Section 6. We assume a  $\Lambda$ CDM cosmology with  $H_0 = 70$  km s<sup>-1</sup> Mpc<sup>-1</sup>,  $\Omega_m = 0.3$ , and  $\Omega_\Lambda = 0.7$ . For this cosmology, 1'' corresponds to  $\sim 7.8$  kpc at  $z = 0.9$  and  $\sim 8.2$  kpc at  $z = 2.3$ . Magnitudes are given in the AB photometric system. A Chabrier (2003) initial mass function (IMF) is adopted throughout.

## 2. OBSERVATIONS AND DATA

### 2.1. Survey Design and Sample Selection

We select KMOS<sup>3D</sup> targets from the 3D-HST Treasury Survey (Brammer et al. 2012; Skelton et al. 2014) in the fields accessible from the VLT (GOODS-S, COSMOS, UDS). The 3D-HST Treasury Survey is a *Hubble Space Telescope* WFC3/G141 grism survey, which provides spectra with resolution of  $R \sim 130$  over  $\lambda = 1.1\text{--}1.7 \mu\text{m}$  in five “deep fields” (COSMOS, GOODS-S, GOODS-N, UDS, and AEGIS). These spectra provide redshifts from continuum breaks and/or emission lines with expected precision of  $\sim 700\text{--}1000$  km s<sup>-1</sup> (Brammer et al. 2012; Whitaker et al. 2013). Where only continuum is measured in the grism the continuum is used to constrain photometric redshifts, based on broadband photometry, by contributing a highly sampled portion of the spectral energy distribution (SED). The grism redshifts rely on rest-frame optical continuum and spectral features and do not require a priori emission line detections. Thus, target selection using 3D-HST grism redshifts effectively reduces the inherent bias toward blue, star-forming, dust-free galaxies of previous rest-frame-UV spectroscopically selected samples at  $z > 1.5$ .

The 3D-HST survey overlaps with the imaging fields of the CANDELS survey, which contributes high-resolution WFC3 near-IR imaging along with Advanced Camera for Surveys imaging for all the KMOS<sup>3D</sup> targets (Grogin et al. 2011; Koekemoer et al. 2011). The fields further benefit from multi-wavelength coverage from the X-ray to far-IR and radio (e.g., Ueda et al. 2008; Lutz et al. 2011; Xue et al. 2011; Civano et al. 2012; Magnelli et al. 2013). The consistency of deep infrared photometry for all targets yields a homogeneous set of SED parameters including stellar mass, UV+IR SFRs, and correction for global dust extinction following Wuyts et al. (2011a).

We assume solar metallicity, the Calzetti et al. (2000) reddening law, and either constant or exponentially declining SFRs. SFRs are determined from the same SED fits or, for objects observed and detected in at least one of the mid-to far-IR (24  $\mu\text{m}$  to 160 $\mu\text{m}$ ) bands with the *Spitzer*/MIPS and *Herschel*/PACS instruments, from rest-UV+IR luminosities through the *Herschel*-calibrated ladder of SFR indicators of Wuyts et al. (2011a). High-resolution (FWHM  $\sim 0.15\text{--}0.20$ ) four-band imaging (*VIJH*) in UDS and COSMOS and seven-band imaging (*BViZJYH*) in GOODS-S provide resolved information of stellar populations, dust extinction, and stellar mass maps that will complement the kinematics, star formation, and nebular emission data derived from KMOS for a combined view of resolved gas and stellar profiles of individual galaxies (Wuyts et al. 2012, 2013; Nelson et al. 2013; Lang et al. 2014).

KMOS<sup>3D</sup> galaxies are selected within three redshift bands that cover  $0.7 \lesssim z \lesssim 2.7$ , where H $\alpha$  emission is located in the *YJ*, *H*, and *K* band filters of KMOS, with a magnitude cut of  $K_s < 23$ . This corresponds to targets being drawn from a 95 per cent mass complete sample at stellar masses,  $\log(M_*[M_\odot]) > 9.65, 10.22, 10.53$  for the redshift ranges  $0.7 < z < 1.1$ ,  $1.2 < z < 1.8$ ,  $1.9 < z < 2.7$ , respectively. We note that the mass completeness is dependent on SFR and thus the values quoted are conservative. At higher SFRs we reach down to lower masses than quoted above.

We use redshift probability functions to avoid contamination of the H $\alpha$ –[NII] complex with OH night skylines and atmospheric absorption windows. For any individual object the effectiveness of the skyline-avoidance criterion is dependent on redshift precision. With the  $K_s$  magnitude cut all galaxies in the resulting sample have either a spectroscopic or grism redshift. For the objects with grism-based redshifts the redshift probability function is conservatively convolved with a  $\pm 1000 \text{ km s}^{-1}$  Gaussian. The location and density of OH skylines are compared with the redshift probability functions for an estimate of the likelihood that H $\alpha$  will be contaminated. Galaxies with the highest probability of contamination are excluded from the sample.<sup>7</sup> The OH and atmosphere avoidance criteria remove  $\sim 70\%$  of possible targets in the full redshift range. The availability of existing spectroscopic redshifts in the planned KMOS<sup>3D</sup> sample is highly dependent on the field. In GOODS-S where a wealth of spectroscopic data are available, 77% of KMOS<sup>3D</sup> target galaxies have a spectroscopic redshift. In contrast, the percentage of target galaxies in COSMOS and UDS that have spectroscopic redshifts is 10% and 13%, respectively.

Further cuts are made based upon grism quality flags as described by Brammer et al. (2012). These additional cuts remove  $\sim 15\%$  of possible targets after the OH avoidance cut. Finally, based upon visual inspection of the grism spectra,  $\lesssim 10\%$  objects are removed due to low-S/N detections of the continuum ( $z_{\text{grism}} \sim z_{\text{phot}}$ ) or overlapping targets in the grism (contaminated continuum flux). The fraction of objects removed for grism contamination is higher in the fields that are dominated by grism redshifts.

### 2.1.1. Survey Strategy

The survey is designed to reach a balance between total number of galaxies and data quality resulting from deep observations necessary to extract high-quality science. All  $z \sim 1, 1.5, 2$

galaxies will be observed for a minimum of four, six, and eight hours, respectively. The large dynamic range in expected H $\alpha$  luminosity of our target sample (factor of  $\sim 1000$ ) requires that longer exposure times for some individual objects to ensure an unbiased sampling of the underlying population. We therefore adopt an observing strategy such that there is significant overlap between adjacent pointings, allowing us to re-observe faint targets and guaranteeing high angular completeness.

In this paper we present the first-year of KMOS<sup>3D</sup> observations, which have largely focused on massive galaxies ( $M_* > 10^{10} M_\odot$ ) with SFRs  $> 0.1 M_\odot \text{ yr}^{-1}$  and  $> 0.2 M_\odot \text{ yr}^{-1}$  in redshift ranges  $0.7 < z < 1.1$  and  $1.9 < z < 2.7$ . The full redshift ranges of our first-year data are  $0.67 < z < 1.04$  and  $2.00 < z < 2.68$  with medians of  $z = 0.90$  and  $z = 2.30$ , respectively. These data sets hereafter will be referred to as the  $z \sim 1$  and  $z \sim 2$  samples.

## 2.2. Observations

KMOS is a multiplexed near-infrared IFS system with 24 deployable  $2.8 \times 2.8$  image slicers over an  $7.2$  diameter patrol field. The IFS units connect to three cryogenic grating spectrometers with  $2k \times 2k$  Hawaii-2RG HgCdTe detectors. The typical spectral resolution,  $R$ , in the *YJ*, *H*, and *K*-band filters used for KMOS<sup>3D</sup> is 3400, 4000, and 4200, respectively. KMOS is a seeing-limited instrument with square  $0.2$  spatial pixels comprising  $14 \times 14$  pixel IFS units.

Observations were prepared with the KMOS Arm Allocator (KARMA; Wegner & Muschielok 2008). Hereafter an individual KARMA setup, or 24 arm allocation, will be referred to as a “pointing.” Each pointing was observed for either 300 s or 600 s using a standard object-sky-object dither pattern, where sky exposures were offset to a clear sky position. Additional subpixel/pixel shifts were included in the object-sky dithering to average over bad pixels. One IFU in each detector is allocated to a star during science observations. The stars are used to monitor the variations in the point-spread function (PSF) and photometric conditions between the observed frames and in each of the three detectors.

Observations were taken during Commissioning on 2013 January 24–25, 29–30, and March 29–31, during P92 on 2014 October 30–November 15, December 7–8, and 2014 January 6–10, and during P93 on 2014 April 19–23 and May 9–10. The observations were taken in good conditions with typical seeing of  $0.6$  in *YJ* and *K* band. Fourteen pointings have been observed, 7 in *YJ* and 7 in *K*. By utilizing overlapping pointings, to allow longer exposure times on certain objects, 37 galaxies have exposure times between 11 and 20 hr. In total 223 galaxies were directly targeted, 106 galaxies at  $z \sim 1$  and 117 galaxies at  $z \sim 2$ . In some cases nearby galaxies were observed within the IFU of the primary target. As a result, 11 additional targets at  $z \sim 1$  and 12 at  $z \sim 2$  were observed for a total of 246 galaxies observed. Of the 23 serendipitous galaxies 6 fit the KMOS<sup>3D</sup> selection criteria outlined in Section 2.1, the remaining 17 fall out of the selection due to likely OH contamination,  $K_s > 23$ , or a bad grism flag. Figure 1 shows the observed galaxies in the SFR– $M_*$  and  $(U - V)_{\text{rest}} - M_*$  planes.

## 2.3. Data Reduction

All data were reduced with the Software Package for Astronomical Reduction with KMOS (SPARK; Davies et al. 2013) using recipes outlined in the SPARK Instructional Guide.<sup>8</sup>

<sup>7</sup> The exact value of this criterion was determined based on previous observations by team members and was found to be appropriate after the first set of KMOS observations.

<sup>8</sup> <ftp://ftp.eso.org/pub/dfs/pipelines/kmos/kmos-pipeline-cookbook-0.9.pdf>

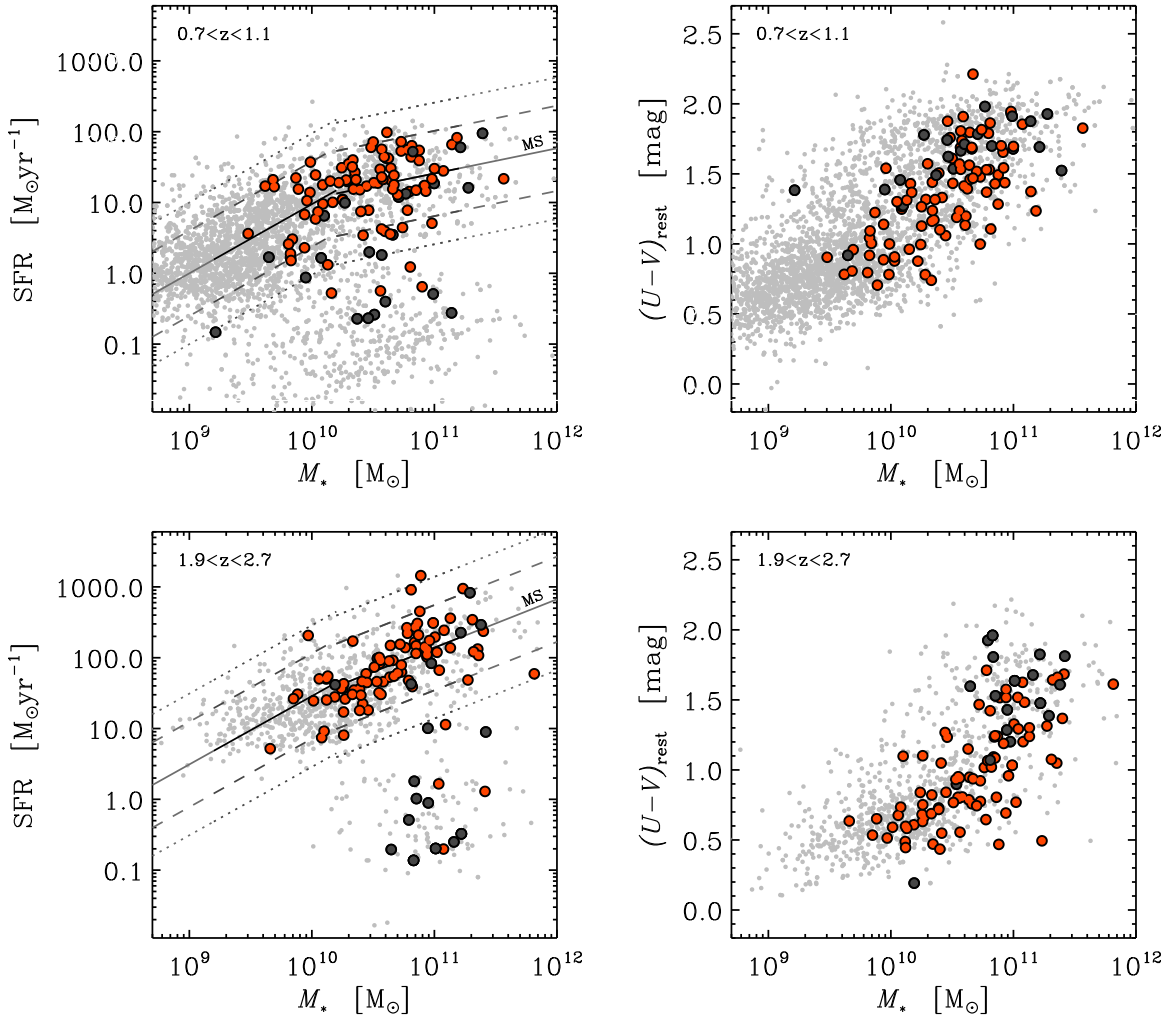


**Figure 1.** Properties of the observed KMOS<sup>3D</sup> sample at  $0.7 < z < 1.1$  (top) and  $1.9 < z < 2.7$  (bottom) in the SFR– $M_*$  plane (left) and  $(U-V)_{\text{rest}} - M_*$  plane (right). Small gray points show the 3D-HST sample without the magnitude and OH contamination selection criterion imposed (Section 2.1). Large red symbols are galaxies that have been observed thus far. Large red symbols are galaxies with H $\alpha$  detections from KMOS and large gray symbols are not detected with the current KMOS data. SFRs are derived from a *Herschel* calibrated ladder of SFR indicators (Wuyts et al. 2011a) and  $M_*$  are derived from SED fits. The broken power-law parameterization, valid between  $\log M_* [M_\odot] = 9.2\text{--}11.2$ , is shown by the solid lines, as defined using 3D-HST data in all CANDELS fields from  $0.5 < z < 2.5$  using UV+IR SFRs (Whitaker et al. 2014). Power-law coefficients for redshifts between the bins given in Whitaker et al. (2014) are obtained through interpolation of the coefficients as a function of stellar mass. Dashed lines and dotted lines show  $4\times$  and  $10\times$  above and below the canonical MS, respectively.

The reduction steps include flat fielding, illumination correction, wavelength calibration, and the sky subtraction technique developed by Davies et al. (2011). Additional processing was done on the raw and reduced data to address known detector issues including removal of the Odd–Even Effect and correction for level offsets in the readout channels.

Individual frames were median combined into final cubes using spatial shifts measured from the average center of the stars within the same pointings. Variations in flux and seeing among the combined frames were typically  $\leq 10\%$  and  $\leq 0''.1$ , respectively.

Estimates of the PSF size for each pointing are made from the average FWHM of the stars included in the pointings. The FWHM of the stars are measured from the combined data cubes using a 2D Gaussian. The star and science observations are simultaneous giving a measurement of the PSF that is consistent with the total time and conditions corresponding to the galaxy data. The mean and median PSF size for the sample presented here is  $0''.62$  and  $0''.58$ , respectively. A more complete analysis

of the PSF for KMOS<sup>3D</sup> observations will be presented by D. Wilman et al. (in preparation).

#### 2.4. Kinematic Mapping

The IDL emission line fitting code LINEFIT is used to derive the kinematic maps from the reduced data cubes (Förster Schreiber et al. 2009; Davies et al. 2011). LINEFIT, originally developed for SINFONI, has been adapted to be used with KMOS data. In short, LINEFIT fits a 1D Gaussian model that is convolved with the instrument’s line-spread function (see below). The fits are performed on all individual continuum subtracted spaxels in the final combined KMOS cubes. The continuum level is determined from two line-free spectral windows around the H $\alpha$ –NII complex. The estimate of the continuum is the mean of the values between the 40th and 60th percentiles, in each window. LINEFIT takes into account the three-dimensional noise properties of the input data via weighting in the fits. The code determines robust and realistic uncertainties on the derived flux and kinematic properties using

Monte Carlo techniques; for more details see Appendix B of Davies et al. (2011).

To correct for instrumental broadening, a Gaussian line profile is created in LINEFIT at the instrumental resolution and then convolved with the model emission line to match the observed profile. Due to differences of resolution in each IFU and along the wavelength axis (Davies et al. 2013), a unique value for the resolution is derived for each object based on which IFU and at which wavelength  $H\alpha$  emission is observed. The resolution is derived from the arc lines and OH sky emission at the same wavelength for the same IFU. For objects observed in multiple IFUs the resolution is determined from the skylines in the unsky-subtracted combined cube for that particular object.

All observations are median filtered spatially with a  $2 \times 2$  pixel box to slightly increase the S/N per pixel without significant loss of spatial resolution. No spectral smoothing or filtering is applied to the data.

In the resulting  $H\alpha$  kinematic maps, pixels where the S/N of  $H\alpha$  drops below  $\sim 5$  are masked out. The kinematic maps on average reach  $2 \times$  the effective  $H$ -band radius. Further pixels are masked for which the line center and width were clearly unreliable based on inspection of the velocity and velocity dispersion maps. The latter masking generally corresponds to the following criteria: velocity and dispersion of a given pixel exceeded by a factor of at least two the typical maximum value over the maps, a velocity uncertainty of  $> 100 \text{ km s}^{-1}$ , and/or a relative velocity dispersion uncertainty of  $> 50\%$ . Continuum maps are constructed for all galaxies.

### 3. RESULTS

From the initial observations presented in this paper, 179 targeted galaxies have  $H\alpha$  emission line detections, 85 detections at  $z \sim 1$  and 94 detections at  $z \sim 2$ , translating into a 80% success rate for targeted galaxies at both redshifts. An additional 12 serendipitous galaxies were detected within the IFUs of targeted galaxies bringing the total number of detections to 191 galaxies (90 at  $z \sim 1$  and 101 at  $z \sim 2$ ). In 77% of the galaxies with  $H\alpha$  emission detected [NII]  $\lambda 6584$  emission is also detected.

Figure 1 shows the location of the KMOS<sup>3D</sup> galaxies with the detected galaxies identified in red. The observed galaxies are shown relative to the underlying 3D-HST parent catalog in SFR, stellar mass, and  $(U - V)_{\text{rest}}$  color for the  $z \sim 1$  and  $z \sim 2$  samples, demonstrating the selection techniques outlined in Section 2.1. At the massive end, where galaxies have been targeted in our initial observations, they closely follow the underlying galaxy population in the SFR- $M_*$  and  $(U - V)_{\text{rest}} - M_*$  planes.

The normalization of the MS is shown at each redshift with a solid line as defined by the broken power-law MS parameterization from Whitaker et al. (2014). The detection fraction is higher on the MS in the SFR- $M_*$  plane, particularly within a factor of  $4 \times$  in SFR of the MS, and for bluer galaxies,  $(U - V)_{\text{rest}} < 1.3$ . However, with current integration times we have also detected a number of galaxies in  $H\alpha$   $10 \times$  below the MS and with  $(U - V)_{\text{rest}} = 1.5\text{--}2.0$  at  $z \sim 1$  and  $z \sim 2$ .

#### 3.1. Redshift Accuracy

The agreement between  $z_{\text{kmos}}$  and  $z_{\text{3D-HST}}$ ,  $|z_{\text{kmos}} - z_{\text{3D-HST}}|/(1 + z_{\text{kmos}})$ , of the detected KMOS<sup>3D</sup> galaxies reflects the redshift accuracy expected from the 3D-HST survey (Brammer et al. 2012). For galaxies selected on a prior spectroscopic redshift and detected with KMOS the median redshift

difference,  $\Delta z/(1 + z)$ , is  $96 \text{ km s}^{-1}$ . For galaxies selected on a grism redshift and detected with KMOS the median  $\Delta z/(1 + z)$  is  $703 \text{ km s}^{-1}$ . Even galaxies with no significant line detection in the grism provide useful constraints for redshifts (Whitaker et al. 2013). Within the KMOS<sup>3D</sup> sample these galaxies have median  $\Delta z/(1 + z)$  of  $1650 \text{ km s}^{-1}$ . We conclude that grism redshifts have an accuracy well suited for KMOS<sup>3D</sup> and provide a significant improvement over photometric redshifts and thus a reliable target sample for our survey.

The detection fraction is marginally higher for galaxies with spectroscopic redshifts in the parent catalog, 85%, than for galaxies with grism redshifts, 78%. While galaxies with grism redshifts are fainter on average and are more often from continuum based redshifts, we do not find a strong trend of the frequency of non-detections or  $\Delta z/(1 + z)$  with target brightness as probed by the F140W magnitudes. The non-detections may be a result of either incomplete observing time with future observations planned (50% of non-detections have incomplete observations) or of large redshift errors shifting  $H\alpha$  outside of the observed band. Within the detected sample 19 galaxies have redshifts from KMOS<sup>3D</sup> deviant from the expected redshift from 3D-HST by  $> 10,000 \text{ km s}^{-1}$  (2 galaxies at  $z \sim 1$  and 17 galaxies at  $z \sim 2$ ).

#### 3.2. Kinematic Measurements

In the following sections, we examine the kinematic properties of our present sample. For all galaxies we derive global properties from the integrated spectrum. For galaxies with  $H\alpha$  emission extending beyond one resolution element (70% of detected galaxies)  $H\alpha$  emission, velocity, and velocity dispersion maps are produced following the procedure in Section 2.4. For resolved galaxies we derive additional parameters from one-dimensional axis profiles extracted along the kinematic major axis, used for kinematic classification in Section 4. The kinematic axis is determined from the 2D velocity field as the direction of the largest observed velocity difference, with the kinematic center defined as the spatial location of the velocity midpoint between the velocity extrema. We measure velocity and velocity dispersion profiles by extracting spectra in apertures equivalent to the size of the average PSF along the kinematic major axis and fit for  $H\alpha$  emission using the LINEFIT code described in Section 2.4. For all galaxies with velocity gradients we measure an observed velocity difference,  $v_{\text{obs}}$ , from the maximal and minimal velocities of the velocity axis profile, such that

$$v_{\text{obs}} = \frac{1}{2}(v_{\text{max}} - v_{\text{min}}). \quad (1)$$

In some cases, typically galaxies that do not show ordered motions, the maximal velocity difference is not along a unique axis passing through the galaxy center. In these cases the maximal and minimal 5% of pixels in the velocity map are used to determine  $v_{\text{max}}$  and  $v_{\text{min}}$ . Kinematic maps with axis profiles are shown for a subset of the KMOS<sup>3D</sup> first-year sample in Figure 12 of the Appendix.

We define two measures of velocity dispersion, the total velocity dispersion and the intrinsic velocity dispersion. The integrated or total velocity dispersion,  $\sigma_{\text{tot}}$ , sometimes referred to as  $\sigma_{\text{net}}$  (e.g., Law et al. 2009), is measured from a single Gaussian fit to the integrated spectrum, or the sum of all the unmasked spaxels and corrected for instrumental broadening. This measurement includes any velocity motions within the galaxy—both resolved and un-resolved. The presence of possible broad ( $\text{FWHM} \geq 500 \text{ km s}^{-1}$ ) emission components from

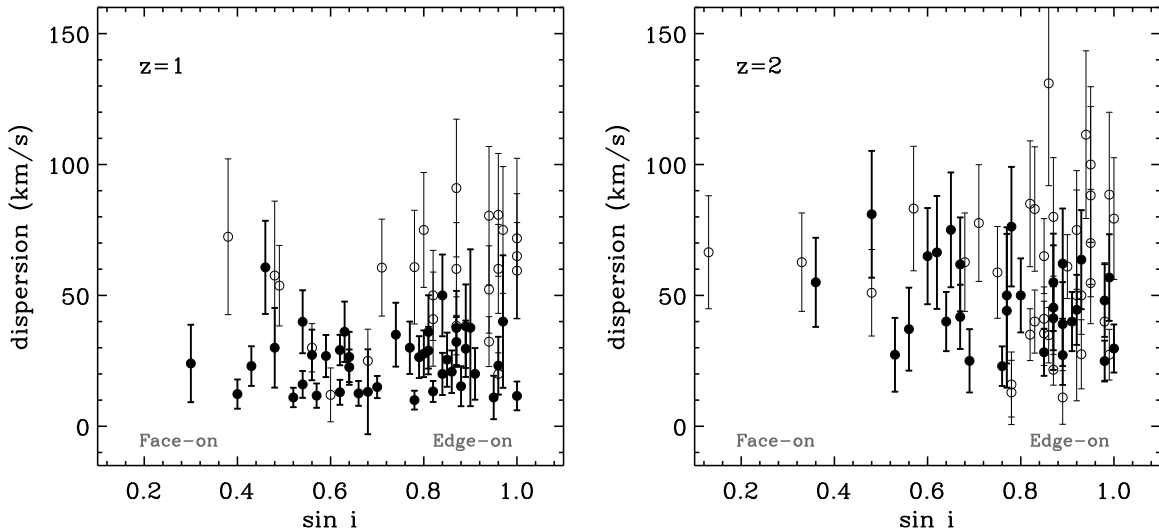


**Figure 2.** Velocity dispersion,  $\sigma_0$ , as a function of inclination for KMOS<sup>3D</sup> galaxies at  $z \sim 1$  (left) and  $z \sim 2$  (right). Disk galaxies, as described in Section 4, with sufficiently high S/N per resolution element to constrain the velocity dispersion in the outer regions of the galaxies are shown by solid circles, the remaining KMOS<sup>3D</sup> galaxies are shown by open circles.

large-scale winds, common in high-redshift galaxies, may inflate  $\sigma_{\text{tot}}$  in such single-Gaussian fits but extensive simulations show that it would be of order 30% or less (Förster Schreiber et al. 2014b).

To obtain an intrinsic measure of velocity dispersion within the galaxies—free of resolved motions and where possible un-resolved motions—we measure  $\sigma_0$  from the outer regions of galaxies, typically along the major-kinematic axis where beam smearing is negligible (e.g., Förster Schreiber et al. 2009, 2014b). Beam smearing is most significant in compact galaxies ( $r_{\text{eff}} \lesssim \text{PSF}$ ) and in the central regions of disk galaxies (Newman et al. 2013). Low S/N in outer regions of rotationally supported galaxies can prohibit the measurement of the intrinsic velocity dispersion where it would be least affected by beam smearing of the steep inner velocity curve—motivating further the prioritization of deep observations for the KMOS<sup>3D</sup> design. Examples of  $\sigma$  axis profiles can be seen in Figure 12 of the Appendix, which confirm for many well-resolved KMOS<sup>3D</sup> galaxies that the velocity dispersion axis profiles flatten at the same radius that the corresponding velocity axis profile flattens. The axis profiles allow measurements slightly beyond the extent of individual spaxels as they are measured from summed spectra within an aperture comparable to the PSF.

We obtain low velocity dispersion measurements for some galaxies in the KMOS<sup>3D</sup> sample ( $\sigma_0 \sim 10 \text{ km s}^{-1}$ ) that are at or below the resolution limit of the observations ( $\sigma_{\text{instr}} = 27\text{--}46 \text{ km s}^{-1}$ ), forcing the question: how far below the spectral resolution limit can the dispersion be reliably measured with KMOS? To investigate this issue, a suite of model emission spectra were created with a uniform distribution of input intrinsic velocity dispersions from  $\sigma_{\text{input}} = 1\text{--}100 \text{ km s}^{-1}$ . The model spectra include noise and skyline residuals matched to the same features in the data. The wavelength position of the emission line is varied in the many iterations. The model spectra are produced with a range of S/N of the emission line, from S/N of 3 to 100, and are convolved with the typical instrumental resolution of the KMOS<sup>3D</sup> observations. To test the ability to recover the input velocity dispersions, the models are fit with Gaussians using LINEFIT following the procedure outlined in Section 2.4.

The recovered dispersion values are in general agreement with the input values of high-S/N models. However, when moving below the resolution element the absolute difference between recovered and input dispersion increases, obtaining on average an overestimate of  $\sigma_{\text{input}}$ . When  $\sigma_{\text{input}} > \sigma_{\text{instr}}$  the recovered dispersions match the input dispersions with a 20% error. When  $\sigma_{\text{input}} \approx \sigma_{\text{instr}}$  the recovered dispersions match the input dispersions with a 30% error. However, when moving from  $\sigma_{\text{input}} \approx \sigma_{\text{instr}}$  to  $\sigma_{\text{input}} \approx 0.3\sigma_{\text{instr}}$  the typical error rises from 30% to 60%. These errors are added in quadrature to the statistical errors of  $\sigma_0$  and  $\sigma_{\text{tot}}$ .

We investigate the possible dependency of measured velocity dispersion with inclination at  $z \sim 1$  and  $z \sim 2$  in Figure 2. At any given point in disk galaxies we observe the line-of-sight velocity dispersion ( $\sigma_{\text{LOS}}$ ), a mixing of the radial component ( $\sigma_R$ ) and vertical component ( $\sigma_z$ ) such that for face-on galaxies  $\sigma_{\text{LOS}} \sim \sigma_z$ . As such,  $\sigma_0$  in the outer regions of more edge-on systems may yield larger measurements along the line-of-sight for disks with  $\sigma_R > \sigma_z$  or unresolved rotation, possibly inflating the  $\sigma_{\text{LOS}}$  (e.g., Aumer et al. 2010). This effect may be enhanced in seeing-limited data due to the larger beam size or compact galaxies where the beam size is a significant fraction of the observed galaxy.

In the low-redshift THINGS survey (Leroy et al. 2008) of H I gas in disk galaxies, a clear increase in dispersion values by  $2\text{--}3\times$  the main locus ( $10\text{--}20 \text{ km s}^{-1}$ ) is seen at high inclinations ( $\sin i > 0.87$ ). Previous analyses of these properties in  $z \gtrsim 1$  kinematic data sets have been either inconclusive (Erb et al. 2004) or do not show a strong trend (Genzel et al. 2011). Figure 2 shows the observed relation for all KMOS<sup>3D</sup> galaxies (open circles) and disk galaxies (as described in Section 4; closed circles). Inclination,  $i$ , is derived from the F160W images, where  $\cos^2 i = (b/a^2 - q_0^2)/(1 - q_0^2)$  and  $q_0 = 0.25$  for a thick disk.

We find no trend between  $\sigma_0$  and inclination at either redshift for the sub-sample of disk galaxies. Inspection of galaxies with dispersions above the main locus at both redshifts reveal compact below-MS galaxies and galaxies where  $\sigma_0$  is an upper-limit due to low S/N at large radii. The lack of a correlation for disk galaxies may be a consequence of a higher fraction of galaxies departing from thin disks at  $z > 1$  (e.g., Reshetnikov

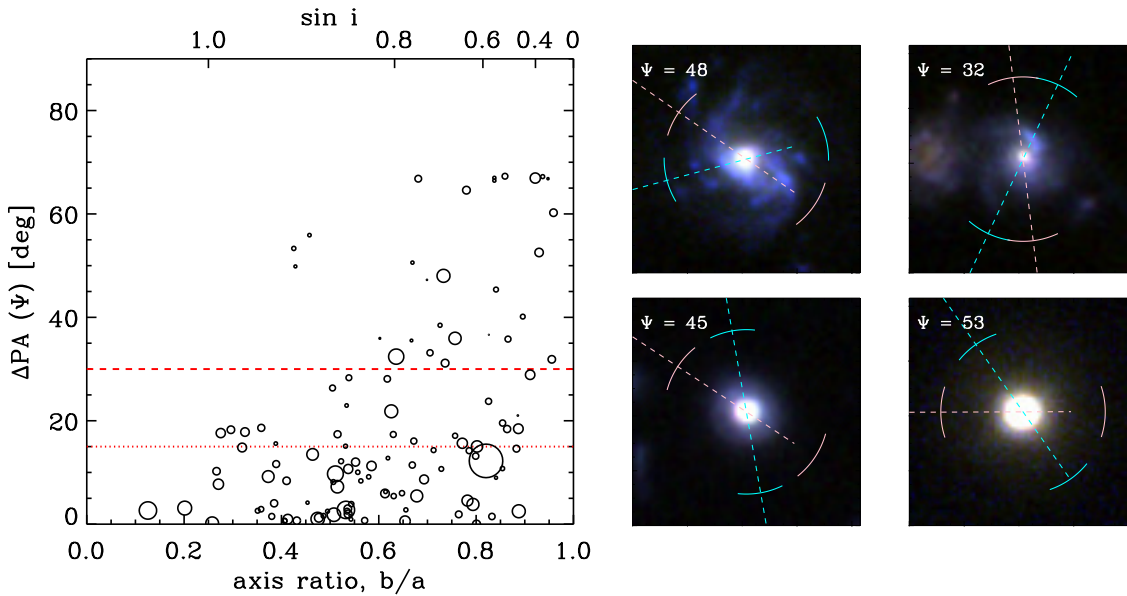


**Figure 3.** Misalignment between photometric and kinematic position angles,  $\Psi$ , as a function of axis ratio,  $b/a$ , measured from F160W *HST* imaging and KMOS kinematic maps, respectively. Symbol size shows the relative size of galaxies in the F160W band. Kinematic and photometric position angles agree within  $15^\circ$  (dotted line) for  $\sim 60\%$  of measurements, while misalignments greater than  $30^\circ$  (dashed lines) are determined for  $\sim 20\%$  of measurements and typically have axis ratios  $> 0.6$ . The right panel shows four examples where  $\Psi > 30^\circ$ , the pink dashed line shows the expected  $\text{PA}_{\text{phot}}$  measured from rest-frame imaging and the cyan dash line shows the kinematic  $\text{PA}_{\text{kin}}$  measured from KMOS data. The arcs are  $36^\circ$  wide, showing  $2\times$  the average difference between kinematic and photometric angles.

et al. 2003; Elmegreen & Elmegreen 2006; Law et al. 2012a; van der Wel et al. 2014a) such that at all viewing angles  $\sigma_{\text{LOS}}$  are a mixing of  $\sigma_{\text{R}}$  and  $\sigma_{\text{z}}$ . Models of disk galaxies of similar size, mass, and intrinsic dispersion to the KMOS<sup>3D</sup> galaxies show that, at the typical S/N of  $\sim 20$ – $40$  of our data sets, the velocity dispersion is well recovered for highly inclined systems but may be underestimated by  $\sim 10\%$  at  $\sin i < 0.8$  (Davies et al. 2011). Accounting for this possible effect would however not change the conclusions from our measurements.

### 3.3. Kinematic to Photometric Misalignments

We compare the derived kinematic position angle from KMOS,  $\text{PA}_{\text{kin}}$ , and the position angle determined from the rest-frame optical imaging (*HST* F160W; van der Wel et al. 2012),  $\text{PA}_{\text{phot}}$ , to determine the reliability of photometric predictions for the kinematic axis and to use for kinematic classification in Section 4. The comparison utilizes the misalignment diagnostic,  $\Psi$ , from Franx et al. (1991);

$$\sin \Psi = |\sin(\text{PA}_{\text{phot}} - \text{PA}_{\text{kin}})|, \quad (2)$$

such that  $\Psi$  is defined as a value between  $0^\circ$  and  $90^\circ$  insensitive to  $180^\circ$  differences between measurement systems. The distribution of misalignments is shown in Figure 3 as a function of photometric axis ratio,  $b/a$ , and  $\sin i$ , for objects where a kinematic major axis can be determined.

The mean and median  $\Psi$  of all galaxies are  $18^\circ$  and  $12^\circ$ , respectively, within the expected errors of both measurements. For 60% of the galaxies the agreement is better than  $15^\circ$  and for 80% of the galaxies the agreement is better than  $30^\circ$ . This comparison demonstrates that the  $\text{PA}_{\text{phot}}$  derived from rest-frame optical photometry provides a reasonable approximation to the  $\text{PA}_{\text{kin}}$  in  $\sim 80\%$  ( $\Psi < 30^\circ$ ) of cases. Of galaxies with  $\Psi > 30^\circ$ , 64% are at  $z \sim 2$ , where galaxy morphologies are often more irregular (the F160W images are probing bluer wavelengths; see Figure 4) and galaxies are often more compact (van der Wel et al. 2014b). The average effective F160W sizes

of the resolved samples are  $r_{\text{eff}} = 5.0$  kpc and  $r_{\text{eff}} = 3.2$  kpc at  $z \sim 1$  and  $z \sim 2$ , respectively.

Among the  $\Psi > 30^\circ$  cases with larger sizes the misalignment can generally be attributed to possible extinction or the influence of sub-structure in morphology such as spiral arms, a central bar, or clump-like features, particularly in face-on systems ( $b/a > 0.6$ ), as seen for two examples on the right-hand side of Figure 3. For the remaining  $\Psi > 30^\circ$  cases that have compact morphologies with little if any low surface brightness features, our data do reveal several cases with clear differential motions of the ionized gas along an axis that would not be predicted based on morphological information alone. These objects in our sample tend to lie at redder colors and below the main sequence—a so far poorly explored part of the  $z = 1$ – $2.5$  galaxy population in IFS surveys.

## 4. GALAXY CLASSIFICATION

The depth and sensitivity of the KMOS<sup>3D</sup> observations allow for the detection of  $\text{H}\alpha$  emission in the outer parts of galaxies essential to constraining kinematic classifications. Robust kinematic classifications not only allow for a better understanding of individual galaxies, but can characterize subsets of galaxies in relation to other key physical properties, e.g., sSFR and stellar structure (e.g., Law et al. 2009, 2012b; Tacchella et al. 2014). Such analyses for large data sets ( $> 100$  galaxies) thus far have primarily been possible with automated morphological parameters (e.g., Sérsic indices; Wuyts et al. 2011b; Law et al. 2012a; van der Wel et al. 2014a) or visual classifications (e.g., Kartaltepe et al. 2012; Hung et al. 2013), which yield similar findings of a MS dominated by disk galaxies with the majority of mergers lying above the MS.

The full KMOS<sup>3D</sup> survey will sample galaxy dynamics across the MS using direct kinematic tracers. The first-year’s worth of KMOS<sup>3D</sup> data, nearly doubling the statistics of existing surveys, already extends kinematic observations to lower sSFR and redder colors for all kinematic types providing a more uniform coverage of the MS. Figures 4–6 show the resolved galaxies

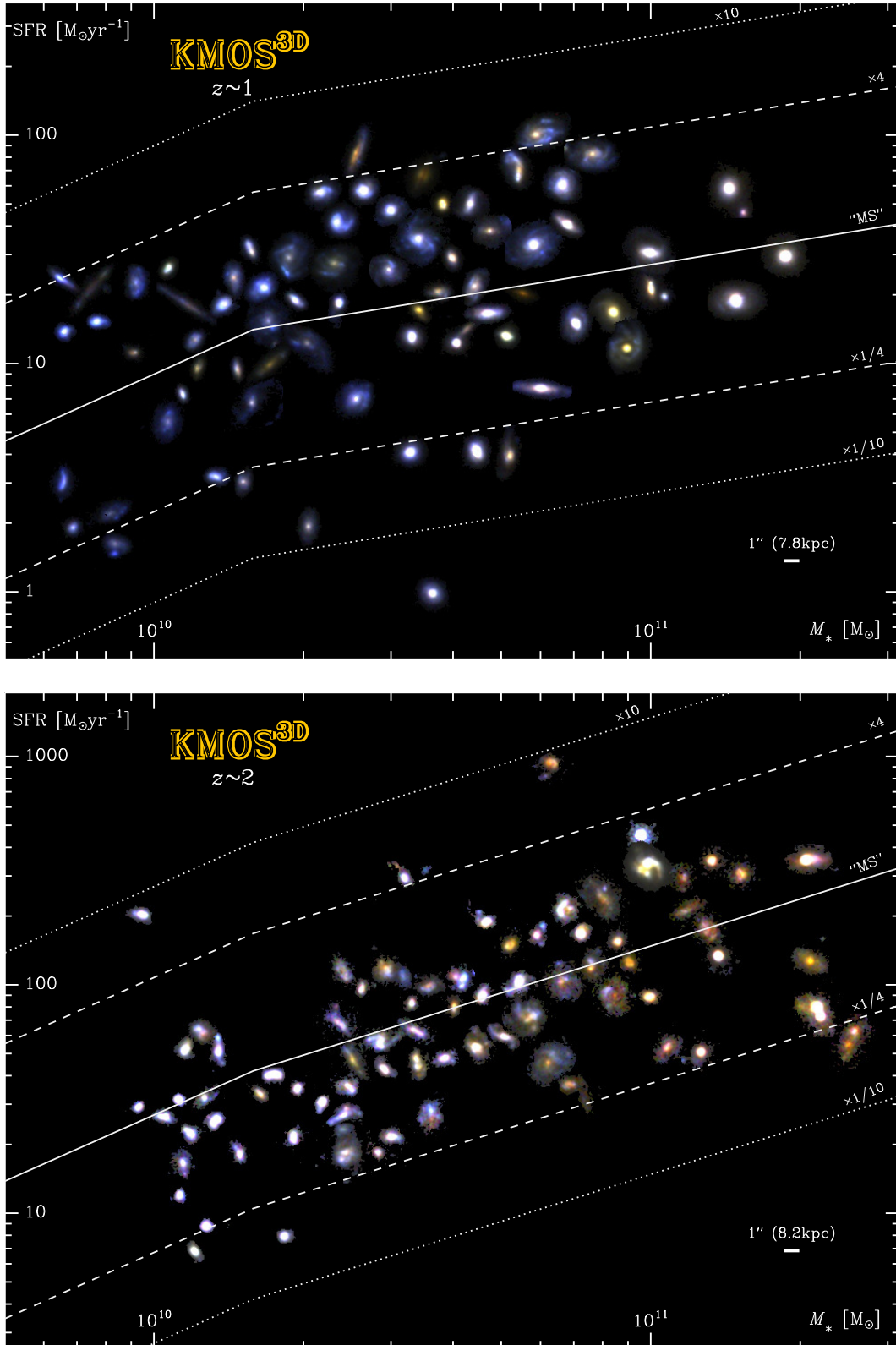


**Figure 4.** Observed-frame *IJH* composite images of the resolved KMOS<sup>3D</sup> galaxies are shown at their approximate locations in the SFR– $M_*$  plane for the  $z \sim 1$  (top) and  $z \sim 2$  (bottom) samples. To avoid overlapping images small offsets are made in the two values to a clean area of parameter space. Offsets are always less than 0.2 dex in either  $M_*$  or SFR, within the typical uncertainties in these properties. The solid line shows the canonical main sequence at  $z \sim 1$  and  $z \sim 2$ , respectively, from Whitaker et al. (2014) adjusted for evolution by interpolating between redshift bins. The dashed and dotted lines show this main sequence scaled up or down by factors of  $\times 4$  and  $\times 1/10$ , respectively. All sources are shown on the same angular scale, as denoted by the 1" scale bar at the bottom right of the plots; the orientation is north up, east left for all objects.

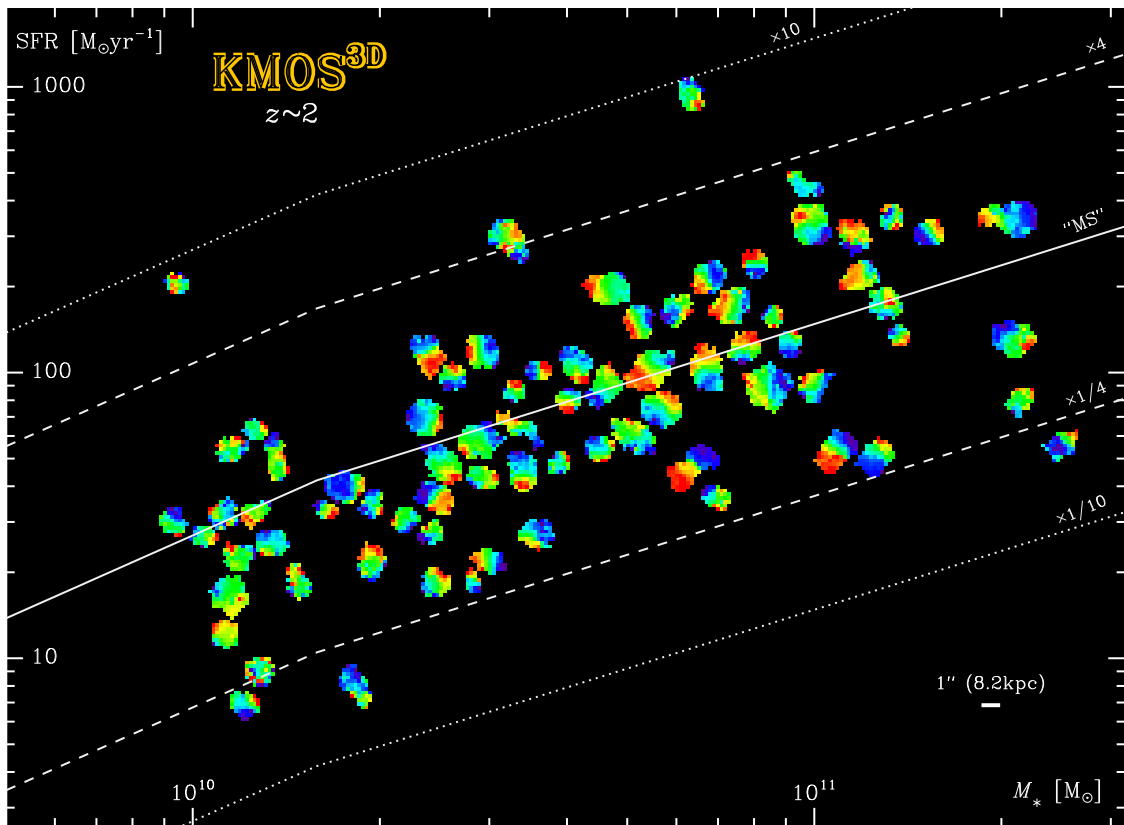
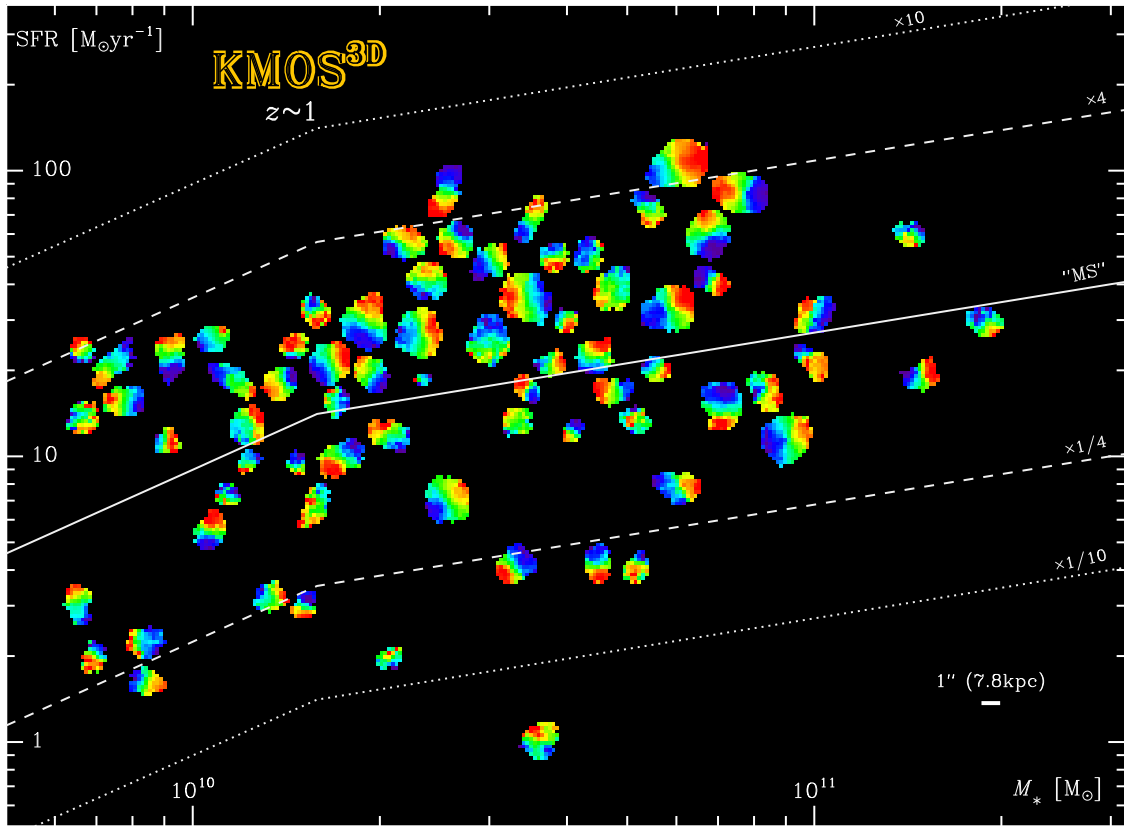


**Figure 5.** KMOS H $\alpha$  velocity fields of the resolved KMOS<sup>3D</sup> galaxies at their approximate locations in the SFR– $M_*$  plane for the  $z \sim 1$  (top) and  $z \sim 2$  (bottom) samples. Positioning of the maps, lines, and labels are the same as in Figure 4.

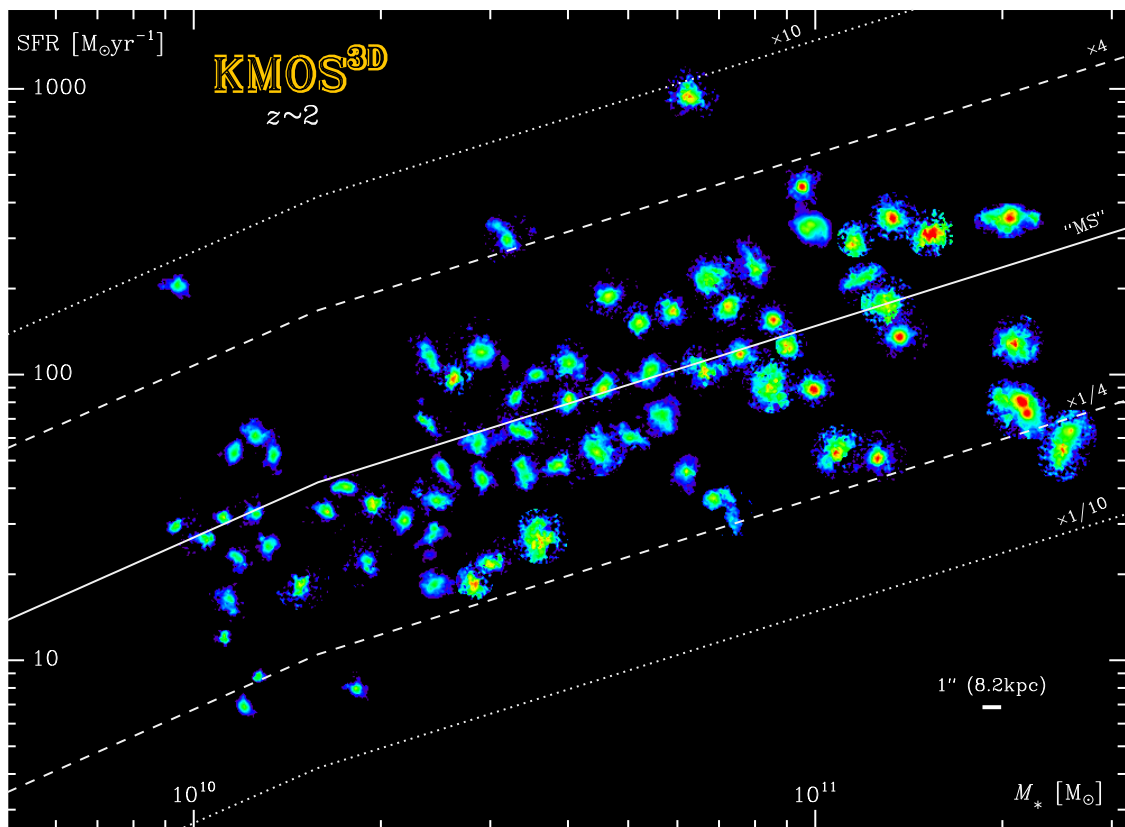
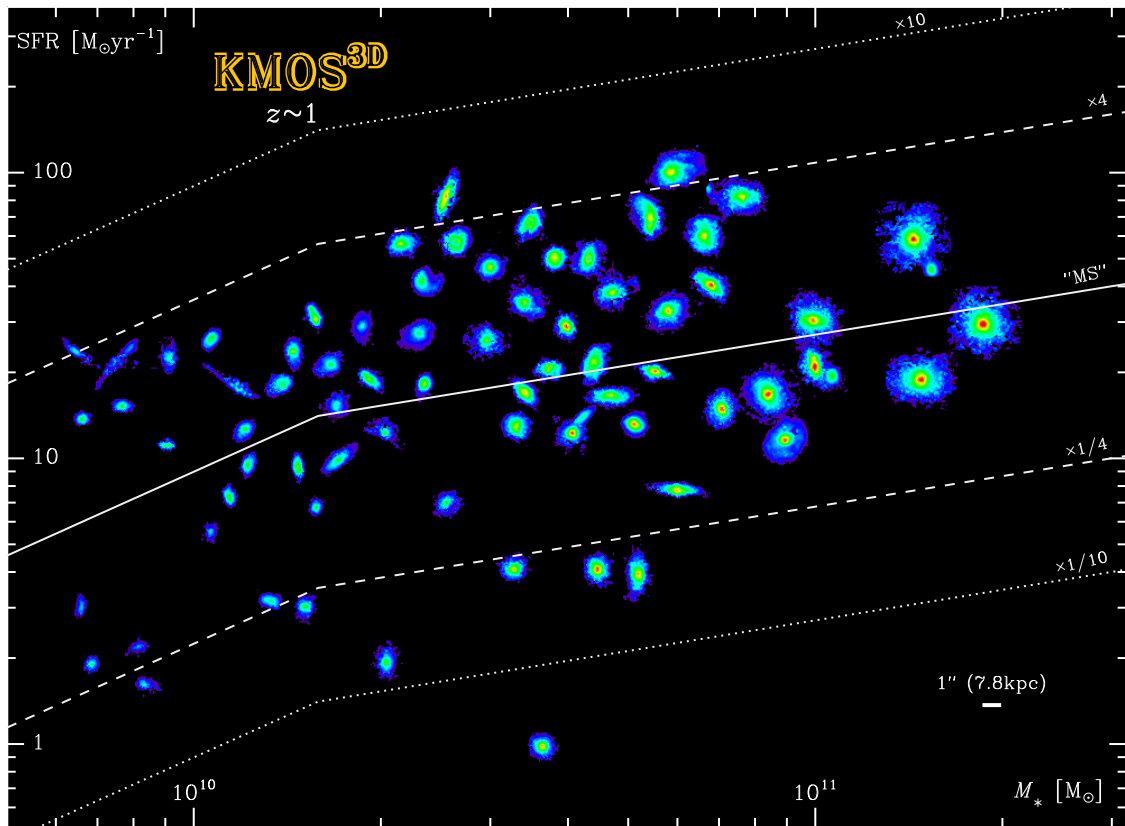


**Figure 6.** Resolved stellar mass maps (Wuyts et al. 2012) of the resolved KMOS<sup>3D</sup> galaxies at their approximate locations in the SFR– $M_*$  plane for the  $z \sim 1$  (top) and  $z \sim 2$  (bottom) samples. Positioning of the maps, lines, and labels are the same as in Figure 4. All mass maps are represented on the same mass–color scale.

**Table 1**  
Percentage of Galaxies Satisfying Disk Criteria

Criteria	1, 2	1, 2, 3	1, 2, 3, 4	1, 2, 3, 4, 5
Full sample	83%	73%	71%	58%
$z \sim 1$	93%	78%	78%	70%
$z \sim 2$	74%	68%	64%	47%

by their color-composite observed-frame *IJH* images, velocity maps, and mass maps at their approximate locations in the  $SFR-M_*$  plane at  $z \sim 1$  and  $z \sim 2$ . A wide variety of photometric morphologies are observed, including galaxies that appear as edge- and face-on disks with little or no central concentration as well as systems with clear bulges. Figures 4 and 6 show the buildup of a central mass concentration, i.e., increasing bulge-to-total ratios when moving to higher galaxy stellar masses reflecting trends of the underlying galaxy population (Lang et al. 2014). This can be connected qualitatively to the velocity maps in Figure 5 as the largest ordered disk-like galaxies that are more often found at high stellar masses.

#### 4.1. Disk Sample

Distinguishing rotationally supported galaxies from other kinematic classes is ideally done through a quantitative analysis, such as kinemetry (e.g., Krajnović et al. 2006). The technique, relying on deviations from symmetries in kinematic maps with respect to that of an ideal rotating disk, is most reliably applied to systems with high S/N over at least  $\sim 10$  resolution elements—suitable for only a small sample of the largest KMOS<sup>3D</sup> galaxies (Shapiro et al. 2008). In the absence of this technique, and in practice yielding the same results, we define disk galaxies by a series of increasingly stricter criteria applicable to the full sample, including compact galaxies (e.g., Newman et al. 2013; Genzel et al. 2014a). The criteria are as follows:

1. the velocity map exhibits a continuous velocity gradient along a single axis (in larger systems this is synonymous with the detection of a “spider” diagram; van der Kruit & Allen 1978);
2.  $v_{\text{rot}}/\sigma_0 > 1$ , where  $v_{\text{rot}}$  is the rotational velocity corrected for inclination,  $i$ , by  $v_{\text{rot}} = v_{\text{obs}}/\sin i$ . These criteria alone are satisfied by 83% of the resolved galaxies, 92% at  $z \sim 1$  and 74% at  $z \sim 2$ . We apply the stricter additional criteria that
3. the position of the steepest velocity gradient, as defined by the midpoint between the velocity extrema along the kinematic axis, is coincident within the uncertainties ( $\sim 1.6$  pixels) with the peak of the velocity dispersion map;
4. for inclined galaxies ( $q < 0.6$ ) the photometric and kinematic axes are in agreement ( $< 30$  degrees);
5. the position of the steepest velocity gradient is coincident, within the uncertainties, with the centroid of the continuum center (a proxy for the center of the potential, i.e., in the higher mass galaxies this is usually a bulge).

In Table 1 we present cumulative disk fractions as each additional criterion is considered. We note that the parameters underlying criteria 4 and 5, photometric PA and continuum center, are sensitive to extinction, sub-structure, and galaxy size. These features can lead to axis misalignment (see Section 3.3) and a shift of the continuum center from the true center of the galaxy potential.

The disk fraction is higher at  $z \sim 1$  than at  $z \sim 2$ , particularly when considering criteria 4 and 5. As discussed in Section 3.3,

and reflected in Table 1, axis misalignment is more common at  $z \sim 2$  where galaxies are more compact and irregular in the observed F160W images. However, the main difference occurs when including criterion 5—coincidence of the kinematic and continuum center—where at  $z \sim 2$  it is possible that extinction and sub-structure, as well as minor-mergers (e.g., Bluck et al. 2009; Hopkins et al. 2010), more frequently influence the measured galaxy centroid. When considering only criteria 1–3, the significance of the different disk fractions between redshift bins, 10%, remains unclear as the size difference between the two redshifts may hinder the detection of small disks at  $z \sim 2$  (Newman et al. 2013).

The inclination,  $i$ , used to estimate the rotational velocity is measured using GALFIT from the rest-frame optical CANDELS images (F160W; van der Wel et al. 2012). However, we note that the inclination derived from photometry will not necessarily correspond to the kinematic inclination, in particular for cases of  $\Psi > 30$  degrees. At high inclinations small errors on  $i$  do not have a large effect on the correction, however for systems with low inclination a small error on  $i$  results in a large error on  $v_{\text{rot}}$ . This uncertainty is explored in detail in a forthcoming paper (S. Wuyts et al., in preparation).

Of the resolved sample 73% fit criteria 1–3, herein the “disk sample”. KMOS<sup>3D</sup> disks are primarily found along the canonical “MS”, extending down to  $10^{9.6}$  and  $10^{10} M_{\odot}$  at the low mass end for  $z \sim 1$  and  $z \sim 2$ , respectively, with five galaxies found below  $1/4 \times$  the MS at  $z \sim 1$ . At  $z \sim 2$  two galaxies are detected significantly above the MS, both of which are compact, consistent with expectations for star-bursting activity (Wuyts et al. 2011b; Bournaud et al. 2011; Elbaz et al. 2011) and are not classified as disks by the above criteria.

In comparison, without the kinematic data a disk fraction is obtained for the resolved KMOS<sup>3D</sup> sample from the photometric data alone using single-component Sérsic fits to the rest-optical photometry (van der Wel et al. 2012). When defining a disk galaxy as having Sérsic index  $n \leq 2.5$ , we find an 83% disk fraction, approximately equal at both redshifts. The photometric disk fraction matches the total fraction of galaxies fulfilling the rotation criteria 1 and 2. Correlating this with our kinematic classifications, six galaxies classified as disks from KMOS data, using all criteria, have  $n > 2.5$ . These galaxies are massive with average  $\log M_* [M_{\odot}] = 11.1$  and visually bulge dominated in their *IJH* images with faint disks or spiral arms (a known effect from comparison with visual classifications; e.g., Kartaltepe et al. 2012).

#### 4.2. Pairs and Mergers

In the current sample 11 targeted galaxies (5 at  $z \sim 1$  and 6 at  $z \sim 2$ ) have possible companions that (1) are in the 3D-HST catalog, (2) are expected to be within the IFU of the primary target (within a projected separation of  $1''.5$  or  $\sim 12$  kpc), and (3) have a redshift such that  $H\alpha$  is expected within  $500 \text{ km s}^{-1}$  of the primary target. The galaxies in “close pairs” fall on the MS at both redshifts. The kinematic maps in which one or both members are detected in  $H\alpha$  show irregularities or non-ordered motions indicating possible mergers. The stellar mass ratios for the close pairs range from 1:1 to 1:15.

The numbers above do not include galaxy pairs with wider spatial separations typically included in merger rate analyses (e.g., Le Fèvre et al. 2000; Lackner et al. 2014), nor do they include mergers in which galaxies are too close to be resolved into multiple objects in the 3D-HST catalogs, but which nevertheless may be classified as mergers based on

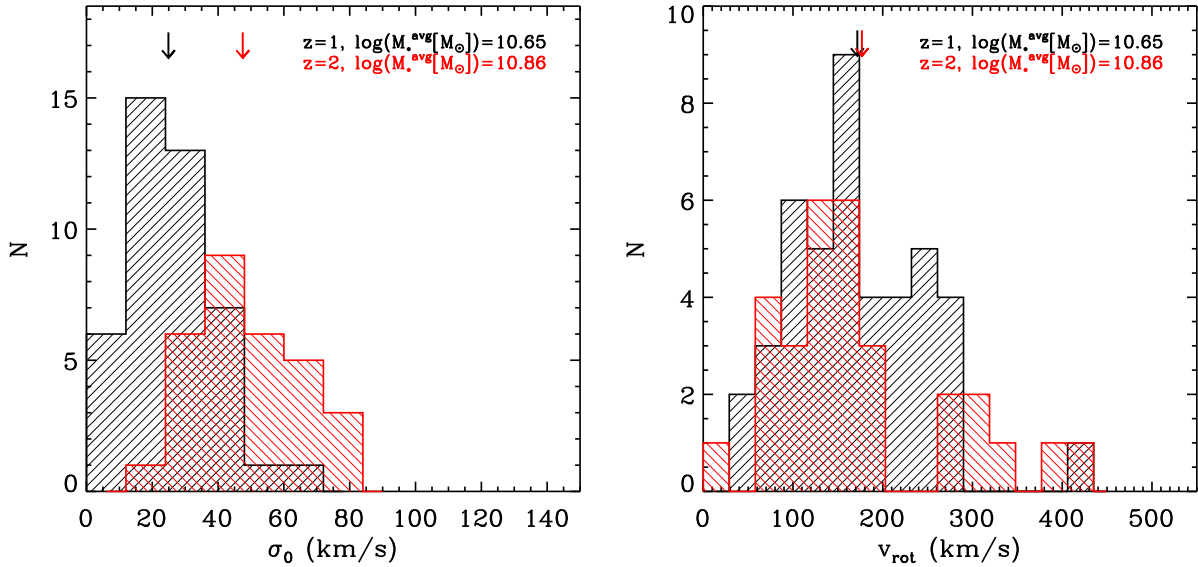


**Figure 7.** Histograms of disk galaxy velocity dispersion,  $\sigma_0$  and  $v_{\text{obs}}$  measurements split into  $z \sim 1$  (black) and  $z \sim 2$  histograms (red). The velocity dispersion and velocity histograms show only galaxies that show rotation and have a reliable  $\sigma_0$  measurement in the KMOS<sup>3D</sup> Survey. The arrows represent the mean values of each distribution. The mean dispersion of the  $z \sim 2$  galaxies is  $2\times$  greater than the mean dispersion of the  $z \sim 1$  population. While there is a  $6\text{ km s}^{-1}$  difference between the average  $z \sim 1$  and  $z \sim 2$  velocity histograms, the populations are mostly overlapping. Average stellar masses for the distributions are  $5 \times 10^{10} M_{\odot}$  and  $7 \times 10^{10} M_{\odot}$  at  $z \sim 1$  and  $z \sim 2$ .

their morphologies (e.g., Lotz et al. 2008; Schmidt et al. 2013; Stott et al. 2013) or kinematics (e.g., COS4\_19753 and COS3\_21583). The kinematics of mergers and galaxy pairs within the sample will be addressed in later papers as the number of observed galaxies increases.

#### 4.3. AGN

No criteria are imposed to exclude galaxies hosting AGNs from the KMOS<sup>3D</sup> sample. AGN incidence at  $z > 1$ , particularly on the MS, is expected to be between 5%–30% at  $\log(M_* [M_{\odot}]) \sim 10$ –12, with the fraction increasing with increasing mass (e.g., Reddy et al. 2005; Daddi et al. 2007a; Brusa et al. 2009; Hainline et al. 2012; Mullaney et al. 2012; Rosario et al. 2012; Bongiorno et al. 2012). As reported in Genzel et al. (2014b), a similar fraction of massive galaxies in the KMOS<sup>3D</sup> sample can be classified as hosting an AGN from X-ray, optical, infrared, and radio AGN indicators. These galaxies are found in a variety of kinematic morphologies, most commonly unresolved or rotating galaxies. One galaxy hosting an AGN is a member of one of the  $z \sim 2$  close pairs.

### 5. VELOCITY DISPERSION OVER COSMIC TIME

Using the two KMOS<sup>3D</sup> redshift slices, we quantify the evolution in ionized gas velocity dispersion from  $z = 2.3$  to  $z = 0.9$ —from the peak of cosmic star formation to the rapid decline. A decrease in intrinsic velocity dispersion has been reported from  $z \sim 1$  to  $z \sim 0$  (Kassin et al. 2012). However, between  $z \sim 2$  and  $z \sim 1$  an accurate measurement of the degree of evolution has not been possible due to a lack of consistent or sizeable data sets (e.g., Epinat et al. 2012; Kassin et al. 2012). For this analysis we use the disk galaxies from KMOS<sup>3D</sup> with sufficiently high S/N per resolution element to constrain the velocity dispersion in the outer regions of the galaxies. Figure 7 shows the distribution of velocity dispersion measurements from these galaxies split into  $z \sim 1$  and  $z \sim 2$  redshift bins. The samples have comparable stellar mass distributions with average  $\log(M_* [M_{\odot}])$  of 10.65 and 10.86, respectively. The means of

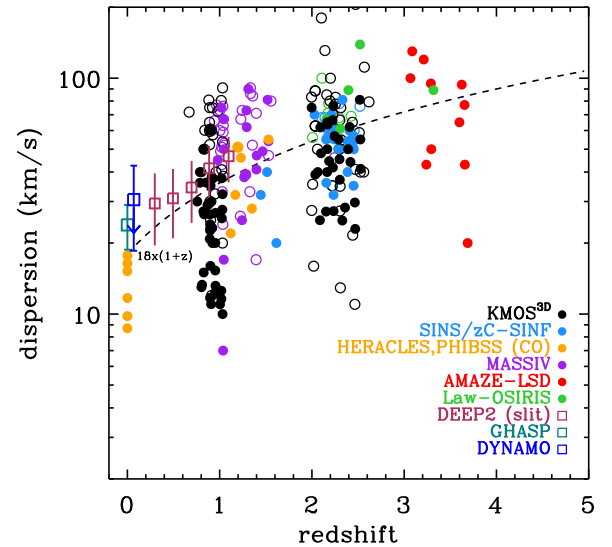


**Figure 8.** Galaxy velocity dispersion measurements from the literature at  $z = 0$ –4 from molecular and ionized gas emission (including IFS and long-slit). KMOS<sup>3D</sup> measurements at  $z \sim 1$  and  $z \sim 2$  are shown by black circles. Filled circles represent disk galaxies or “rotators,” open circles represent all other kinematic categories. Open squares are averages of surveys at  $z \lesssim 1$ . Sources for the literature data are given in Section 5. The dashed line shows a simple  $(1+z)$  evolution scaled by a factor of  $18\times$  to overlap with the data.

each  $\sigma_0$  distributions are  $24.9\text{ km s}^{-1}$  and  $47.5\text{ km s}^{-1}$  as shown by the downward arrows—a factor of  $2\times$  evolution for disk galaxies from  $z \sim 2$  to  $z \sim 1$ . In contrast, the rotational velocity,  $v_{\text{rot}}$ , distributions are comparable in their peaks and widths with a measured difference of the means at  $z \sim 1$  and  $z \sim 2$  of  $6\text{ km s}^{-1}$ .

In Figure 8 we examine the evolution of velocity dispersion determined from KMOS<sup>3D</sup> within the wider redshift range of IFS samples across  $z = 0$ –4, including all galaxy types with dispersions measured from the ionized gas via  $\text{H}\alpha$  or  $[\text{OIII}]$  and molecular gas via millimeter interferometric observations of CO. While the scatter is large, there appears to be an

approximate  $1+z$  evolution in measured velocity dispersion across cosmic time.

The data included in Figure 8 at  $z \gtrsim 1$  are from the MASSIV survey ( $\log M_*^{\text{avg}}[M_\odot] = 10.2$ ; Epinat et al. 2012; Vergani et al. 2012), SINS/zC-SINF survey ( $\log M_*^{\text{avg}}[M_\odot] = 10.6$ ; Förster Schreiber et al. 2009, 2014b), OSIRIS survey from Law et al. (2009) ( $\log M_*^{\text{avg}}[M_\odot] = 10.3$ ), and AMAZE-LSD surveys ( $\log M_*^{\text{avg}}[M_\odot] = 10.1$ ; Gnerucci et al. 2011). At  $z < 1$  averages are shown by open squares for the GHASP sample (Epinat et al. 2010;  $\log M_*^{\text{avg}}[M_\odot] = 10.6$ ), and the “MS” DYNAMO galaxies at  $z < 0.1$  (Object classes A-C and E;  $\log M_*^{\text{avg}}[M_\odot] = 10.3$ ; Green et al. 2014). Velocity dispersions derived from molecular gas are included from the  $z = 1-2$  PHIBSS survey ( $\log M_*^{\text{avg}}[M_\odot] = 11.0$ ; Tacconi et al. 2013) and at  $z = 0$  from the HERACLES survey ( $\log M_*^{\text{avg}}[M_\odot] = 10.5$ ; Leroy et al. 2008, 2009).

The DEEP2 survey is the only long-slit survey included in Figure 8, due to its wide redshift range ( $z = 0.2-1.2$ ) and reported dispersion evolution for galaxies of  $10^8-5 \times 10^{10} M_\odot$  (Kassin et al. 2012). We note that long-slit data may report high dispersion values due to PA uncertainties and lack of spatial information but is similar in general to the “along the slit” method used to derive  $\sigma_0$ .

A source of scatter within the samples shown in Figure 8 may originate from measurement uncertainties in determining the intrinsic velocity dispersion or when  $\sigma_0$  is close to or below the instrumental resolution as discussed in Section 3. Furthermore, dispersions of disturbed systems or non-disk systems may be probing different physics than dispersions of disk galaxies; e.g., mergers may enhance  $\sigma_0$  (Bournaud et al. 2011; Powell et al. 2013; Arribas et al. 2014). For galaxies showing rotation but for which a flattening in velocity, as expected for disks, has not been reached the measured dispersion is an upper limit and will be higher than the intrinsic dispersion. Indeed, while considering only the disk galaxies satisfying all criteria in Section 4 with  $\sigma_0$  measurements constrained in the galaxies outer regions, the scatter of dispersion in the KMOS<sup>3D</sup> samples is reduced.

Differences between samples can also arise from diverse selection criteria, spatial and spectral resolution, stellar mass ranges, and measurement methods that could bias the interpretation of evolution. The KMOS<sup>3D</sup> dispersion values are measured with the same methods as the SINS/zC-SINF, PHIBSS, and HERACLES surveys, using the outside of the disk kinematics free of beam-smearing. The MASSIV survey uses a beam-smearing corrected error-weighted mean of the dispersion map that should give values consistent with  $\sigma_0$ , however the difference in methods could lead to the higher mean dispersions from the MASSIV galaxies. The GHASP dispersions are calculated from the average of the 20% lowest dispersion spaxels from the dispersion maps, a method consistent with  $\sigma_0$  when there are a sufficient number of spaxels in the map. AMAZE/LSD subtract a dynamical disk model from the observed dispersion map to correct for galaxy rotation and give an average of the results. The flux weighted mean of the dispersion map was used to derive a global  $\sigma$  for Law et al. (2009) and DYNAMO (Green et al. 2014) and is known to give systematically higher values (Davies et al. 2011), although Green et al. (2014) do include a beam smearing correction.

Spectral and spatial resolution limits of the high-redshift surveys are comparable. The MASSIV, AMAZE/LSD, and SINS/zC-SINF surveys were observed with SINFONI in both seeing limited and AO resolution modes ( $R = 3000-5000$ , pixel scale =  $0.05 - 0''.25$ ). KMOS has comparable sensitivity

and spectral and spatial resolution as SINFONI in seeing-limited mode. The Law et al. (2009) sample taken with OSIRIS, a similar AO instrument on the Keck Telescope, has spatial sampling of  $0''.05$  and comparable spectral resolution. The resolution of the DEEP2 spectra, spanning from  $z = 0.2-1.2$ , is  $R \sim 5000$  ( $\sigma = 25.5 \text{ km s}^{-1}$ ), which may hinder some measurements of  $\sigma$  in the lower-redshift regime, possibly underestimating the degree of the overall evolution.

At  $z < 1$  there is more variety among the resolution of the samples. The spectral and spatial resolutions of the  $z \sim 0$  GHASP and HERACLES surveys are  $3-13 \text{ km s}^{-1}$  and  $\sim 0.3-0.5 \text{ kpc}$ , respectively, providing reliable measurements of intrinsic velocity dispersions in the outer regions of disk galaxies. The  $z \sim 0.01$  DYNAMO sample has comparable spectral resolution of  $15 \text{ km s}^{-1}$ , but poorer spatial resolution ( $\sim 3 \text{ kpc}$ ) leading to possible beam smearing effects. Indeed, recent work with higher spatial resolution ( $\sim 1 \text{ kpc}$ ) of two DYNAMO disk galaxies reveal  $30$  and  $37 \text{ km s}^{-1}$  in the outer disks compared to the originally reported beam-smearing corrected integrated dispersions of  $50$  and  $45 \text{ km s}^{-1}$ , respectively (Bassett et al. 2014). The measurement technique presented in Bassett et al. is more in line with  $\sigma_0$ , and thus the percent reduction derived from the two galaxies is reflected in Figure 8 with a downward arrow.

### 5.1. Trends with Other Observed Properties

As galaxies buildup their mass and size (depleting their gas reservoirs) they become more stable to small perturbations from gas accretion, galactic winds, and/or minor mergers (Martig et al. 2009; Genzel et al. 2014a; Tacconi et al. 2013). Assuming this scenario, we investigate possible correlations between turbulence and disk stability ( $v_{\text{rot}}/\sigma_0$ ) with  $M_*$ , sSFR,  $\Delta\text{SFR} = \log(\text{SFR}/\text{SFR}_{\text{MS}})$ , and gas fractions ( $f_{\text{gas}}$ ) that may account for the scatter of KMOS<sup>3D</sup> galaxies in Figure 8.

Spearman rank correlation coefficients and significance levels for the six panels of Figure 9 reveal that  $M_*$ , sSFR,  $\Delta\text{SFR}$ , and  $f_{\text{gas}}$  are more strongly correlated with  $v_{\text{obs}}/\sigma_0$  than  $\sigma_0$  when considering the full redshift range of the current disk sample. The strongest correlation with dispersion as measured by the Spearman coefficient is with  $\Delta\text{SFR}$  in the  $z \sim 2$  sample with  $\rho = 0.45$  with  $2.5\sigma$  significance level, hinting at a possible trend of an increasing velocity dispersion when moving above the MS at a fixed mass. This trend however is absent at  $z \sim 1$  putting the already low significance at  $z \sim 2$  in question. When both redshift regimes of the KMOS<sup>3D</sup> disk sample are considered together a weak correlation ( $\rho = 0.31$  at  $2.5\sigma$ ) is measured between  $M_*$  and  $\sigma$ . However, within individual redshift slices the dynamic range in  $M_*$  of the first-year data is limited.

The strongest correlation when considering the combined  $z \sim 1-2$  sample is between  $v_{\text{obs}}/\sigma_0$  and sSFR ( $\rho = 0.48$  at  $4\sigma$ ), which may contribute to the evolution between samples in Figure 8 due to the known evolution of sSFR. The next strongest correlation is between  $v_{\text{obs}}/\sigma_0$  and  $f_{\text{gas}}$  ( $\rho = 0.40$  at  $3\sigma$ ) where  $f_{\text{gas}}$  is derived from the galaxies redshift and SFR following Tacconi et al. (2013). A correlation between  $v_{\text{obs}}/\sigma_0$  and  $f_{\text{gas}}$  was also reported in Newman et al. (2013) and is in line with predictions from models that suggest accretion energy would drive up both disk turbulence and gas fractions (e.g., Elmegreen & Burkert 2010). Given the tight inter-relationship between  $f_{\text{gas}}$ , sSFR and  $\Delta\text{SFR}$  (e.g., Tacconi et al. 2013; Genzel et al. 2014c), it is perhaps unsurprising that kinematic properties of the gas are found to correlate with all three parameters. The connection of disk velocity dispersion on sSFR and  $f_{\text{gas}}$  are explored more in the next section.

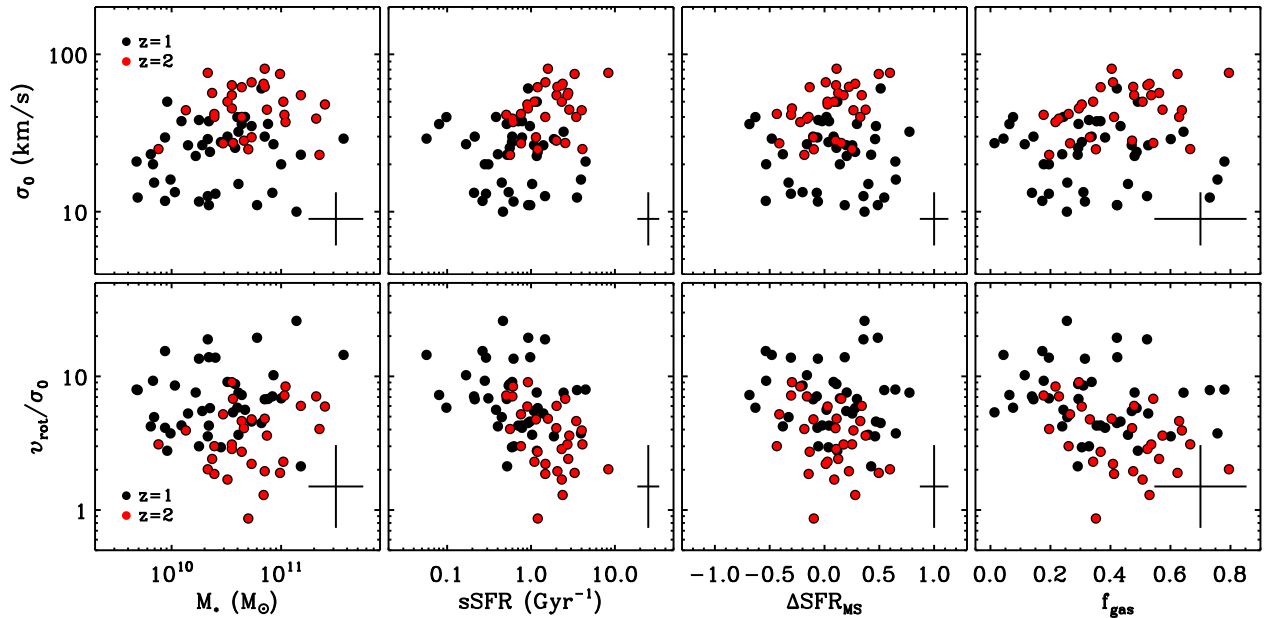


**Figure 9.** Disk velocity dispersion,  $\sigma_0$ , and disk stability,  $v_{\text{rot}}/\sigma_0$ , for the KMOS<sup>3D</sup> first-year disk sample as a function of  $M_*$ , sSFR,  $\Delta\text{SFR}_{\text{MS}}$ , and  $f_{\text{gas}}$  at  $z \sim 1$  (black points) and  $z \sim 2$  (red points). Representative error bars for individual points are shown at the lower right of each plot.

### 5.2. Velocity Dispersions in the Context of Galaxy Evolution

Both outflows and accretion are predicted to be prevalent at the high redshifts where large internal motions are measured. Outflows are observed to be common at high redshift ( $z \sim 1-3$ ) from star formation and AGNs (Nesvadba et al. 2008; Weiner et al. 2009; Shapiro et al. 2009; Steidel et al. 2010; Nestor et al. 2011; Harrison et al. 2012; Newman et al. 2012; Förster Schreiber et al. 2014; Genzel et al. 2014b). While accretion has yet to be directly observed, a consequence of the expected accretion is larger molecular gas content and higher sSFRs at early times, with the evolution of both quantities established observationally (molecular gas fractions: Tacconi et al. 2010, 2013; Daddi et al. 2010; Combes et al. 2011; Genzel et al. 2014c; sSFR: Bouché et al. 2010; Dutton et al. 2010; Whitaker et al. 2012b, 2014; Stark et al. 2013; González et al. 2014). However these mechanisms and their evolution are not exclusive, but rather essential elements of the equilibrium or regulator model in which SFGs are well described as being in a fairly steady equilibrium between inflows, star formation, and outflows (Bouché et al. 2010; Davé et al. 2012; Lilly et al. 2013; Dekel & Mandelker 2014).

We use the first-year of KMOS<sup>3D</sup> data in tandem with data from the literature to test the scenario that the evolution of velocity dispersion is consistent with the equilibrium model and is primarily a result of the gas inflow onto galaxies, most efficient at high redshifts. We derive a scaling for velocity dispersion for near-critical disks as a function of redshift using the evolution of molecular gas fractions, depletion time ( $t_{\text{dep}}$ ), and specific SFR using recent observational results in the literature that are independent of the IFS data discussed thus far.

We derive the expected gas fraction evolution of SFGs at a given stellar mass, where the gas fraction is defined as

$$f_{\text{gas}} = \frac{1}{1 + (t_{\text{dep}}\text{sSFR})^{-1}} \quad (3)$$

(Tacconi et al. 2013).

To rewrite Equation (3) as a function of redshift, we use the evolution of depletion time described by

$$t_{\text{depl}}[\text{Gyr}] = 1.5 \times (1+z)^\alpha, \quad (4)$$

with  $\alpha$  measured to be  $-0.7$  to  $-1.0$  by Tacconi et al. (2013), and predicted to be  $-1.5$  in the analytic model of Davé et al. (2012). For simplicity and consistency with Tacconi et al. (2013)  $\alpha = -1$  is adopted. The leading factor of 1.5 Gyr is a normalization to the typical depletion time observed in local galaxies (Leroy et al. 2008; Bigiel et al. 2011; Saintonge et al. 2012). Using the cosmic decline of specific SFR defined at  $0.5 < z < 2.5$  from Whitaker et al. (2014),

$$\text{sSFR}(M_*, z) = 10^{a(M_*)} (1+z)^{b(M_*)}, \quad (5)$$

where we fit to the constants in Table 5 of Whitaker et al. (2014) to describe  $a$  and  $b$  as a function of stellar mass, such that

$$a(M_*) = -10.73 + \frac{1.26}{1 + e^{(10.49 - \log M_*)/(-0.25)}},$$

$$b(M_*) = 1.85 + \frac{1.57}{1 + e^{(10.35 - \log M_*)/0.19}}. \quad (6)$$

Equation (6) is valid in the  $M_*$  range of  $\log M_* [M_\odot] = 9.2-11.2$  constrained by the data.

The evolution of the  $t_{\text{depl}}$  and evolution of sSFR are strongly linked (Saintonge et al. 2011; Tacconi et al. 2013; Genzel et al. 2014c). For simplicity we use the above relations to derive the evolution of gas fractions. We note that our results are consistent with adopting  $t_{\text{depl}}$  from Genzel et al. (2014c). Furthermore, at  $z \gtrsim 3$  the evolution of sSFR is debated (Stark et al. 2013; González et al. 2014) with different behaviors expected from different models or extrapolating fits to data beyond where they are constrained. Equation (5) is unconstrained at  $z > 2.5$ , but the resulting extrapolation is roughly consistent with published measurements out to  $z \sim 4$  (e.g., Bouwens et al. 2012; Stark et al. 2013).

By considering only disk galaxies a prediction for the evolution of ionized gas velocity dispersions can be derived by

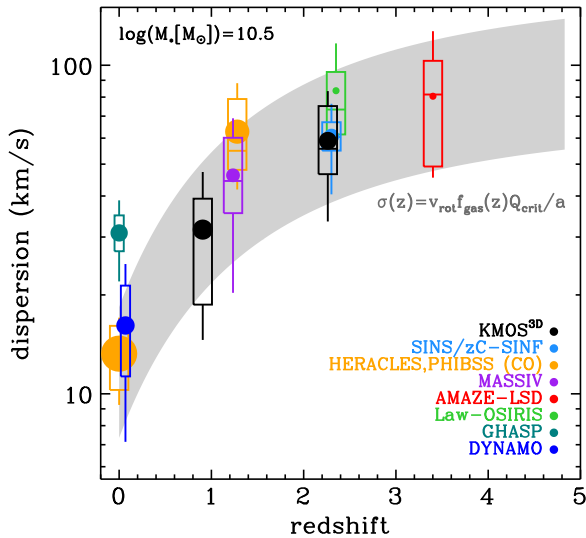


**Figure 10.** Same as Figure 8 but showing the medians (horizontal lines) and means (circles) of samples that have high-resolution IFS data, their 50% distributions (boxes) and 90% distribution (vertical lines). The points representing each sample are sized to the average relative half-light size of the galaxies and adjusted using Equations (3)–(6) to an average  $\log(M_*) = 10.5$ . The gray band is described by  $\sigma_0 = v_{\text{rot}} Q_{\text{crit}} f_{\text{gas}}(z)/a$  where  $f_{\text{gas}}(z)$  is the gas fraction as a function of redshift as determined by Equations (3)–(7),  $Q_{\text{crit}} = 1$  and  $a = \sqrt{2}$  for a  $\log(M_*) = 10.5$  disk with constant rotational velocity. The upper and lower boundaries of the curves are defined by  $v_{\text{obs}} = 250$  and  $100 \text{ km s}^{-1}$ , respectively.

rewriting the Toomre stability criterion (Toomre 1964) as

$$\frac{v_{\text{rot}}}{\sigma_0} = \frac{a}{f_{\text{gas}}(z) Q_{\text{crit}}}, \quad (7)$$

where  $a = \sqrt{2}$  for a disk with constant rotational velocity and  $Q_{\text{crit}} = 1.0$  for a quasi-stable thin gas disk (Förster Schreiber et al. 2006; Genzel et al. 2011). As a result, disk velocity dispersion is expected to evolve directly with the gas fraction:

$$\sigma_0(z) = \frac{1}{\sqrt{2}} v_{\text{rot}} f_{\text{gas}}(z). \quad (8)$$

Figure 10 shows the average velocity dispersions for disk galaxies only, taken from IFS surveys with good spatial and spectral resolution. The prediction for the evolution of dispersion for  $\log M_* = 10.5$  galaxies using the above assumptions is shown by the gray band, bounded by  $v_{\text{obs}} = 100\text{--}250 \text{ km s}^{-1}$  corresponding to the approximate spread of the peak of  $v_{\text{rot}}$  in Figure 7. The spread in  $\sigma_0$  values for each survey, their 50% distributions and 90% distributions, are shown by the boxes and vertical lines, respectively.

The observed dispersions and predicted evolution are in remarkably good agreement indicating that the evolution of measured velocity dispersions can be described by the evolution of key properties ( $f_{\text{gas}}$ ,  $t_{\text{dep}}$ , sSFR) consistent with the equilibrium model. While correlations between  $v/\sigma_0$ ,  $\sigma_0$ ,  $f_{\text{gas}}$ , and sSFR are uncertain due to a lack of dynamic range and large errors on individual measurements in Figure 9, by expanding to the wider redshift range and using the global scaling for  $f_{\text{gas}}$  (rather than inferring it for individual galaxies from other observed parameters) the influence of a more active and gas-rich environment on velocity dispersion is seen in Figure 10.

Some caveats arise from assumptions made in the derivation for the adopted stellar mass, rotational velocity range, and

critical Toomre parameter. For instance, the sSFR is dependent on stellar mass (e.g., Damen et al. 2009; Bouché et al. 2010; Whitaker et al. 2014) and the samples included in the analysis have average stellar masses ranging from  $\log M_* = 9.4\text{--}11.0$ . For a comparison at the same stellar mass, we adjust the average velocity dispersion for each sample to a reference stellar mass of  $\log M_* = 10.5$  using the ratio of Equation (3) solved at the reference mass and the average mass of the sample. The average absolute adjustment is  $5 \text{ km s}^{-1}$  with the largest adjustment being to the PHIBSS sample ( $25 \text{ km s}^{-1}$ ), which has an average stellar mass of  $\log M_* = 11.0$ .

The expected range of velocity dispersions at a given redshift can be widened by increasing the range of rotational velocities considered in Equation (8). The boundary values of  $100 < (v_{\text{obs}}[\text{km s}^{-1}]) < 250$  are used in Figure 10 to encompass the peaks of the  $z \sim 1$  and  $z \sim 2$  histograms of rotational velocities of the KMOS<sup>3D</sup> galaxies in Figure 7 and are consistent with the other surveys considered with the exception of the sample of Law et al., which has average  $v_{\text{rot}} = 50 \text{ km s}^{-1}$ .

We have made the assumption that all disk galaxies considered for this analysis are quasi-stable disks with  $Q_{\text{crit}} = 1.0$ , the value derived for a pure thin gas disk. However, the critical Toomre parameter is 0.67 for a thick gas disk and increases by factors 1–2 for a stellar-plus-gas disk (e.g., Kim & Ostriker 2007). There are indications from our data and the literature that disk galaxies at  $z \sim 1\text{--}2$  are both thick (e.g., Elmegreen & Elmegreen 2006; Genzel et al. 2011) and composite (e.g., Lang et al. 2014); thus, we adopt  $Q = 1$  as an acceptable average value. Increasing  $Q_{\text{crit}}$  to  $Q = 2$ , as may be expected toward lower redshifts where stellar disks could play a more significant role in the stability of the system, would more than double the predictions for measured velocity dispersion. The resulting prediction would be consistent with the  $z \sim 0$  GHASP sample (Figure 8), which lies above the prediction in Figure 10.

To further test the validity of the assumption of  $Q = 1$ , we use the observed  $(v_{\text{rot}}/\sigma)$  for disk galaxies, which is expected to be nearly constant over cosmic time in balance with  $a/(f_{\text{gas}} Q_{\text{crit}})$  from Equation (7) as shown in Figure 11. Here  $Q_{\text{crit}}$  is varied between 0.67 and 2 to account for the difference between thin and thick gas disks and composite gas plus stellar disks. All  $z \gtrsim 1$  samples are consistent with  $Q = 1$ , although in most cases the full distribution of the sample encompasses a range of  $Q$  values. The  $z = 0$  surveys are in better agreement with  $Q = 2$ . To extract more conclusive  $Q_{\text{crit}}$  values, and/or a possible evolution in  $Q_{\text{crit}}$ , observations with gas fractions measured on a galaxy-by-galaxy basis directly from molecular tracers are needed.

## 6. CONCLUSIONS

This paper presents the design and first results of KMOS<sup>3D</sup>, a deep integral field spectroscopic survey targeting  $>600$   $z = 0.7\text{--}2.7$  galaxies, being carried out over the next  $\sim 5$  yr with KMOS on the VLT. KMOS<sup>3D</sup> is designed to be a representative survey with a simple coherent selection from a comprehensive mass-selected parent catalog with redshifts from the near-infrared 3D-HST grism survey. The survey pushes well below the MS of star formation to characterize the internal dynamics and star formation of galaxies transiting from star forming to passive.

To date 246 galaxies have been observed for the KMOS<sup>3D</sup> survey with observing times ranging from 2 to 20 hr. A total of 191 galaxies with  $M_* > 4 \times 10^9 M_{\odot}$  are detected in H $\alpha$  with KMOS: 90 galaxies at  $z \sim 1$  and 101 galaxies at  $z \sim 2$  with

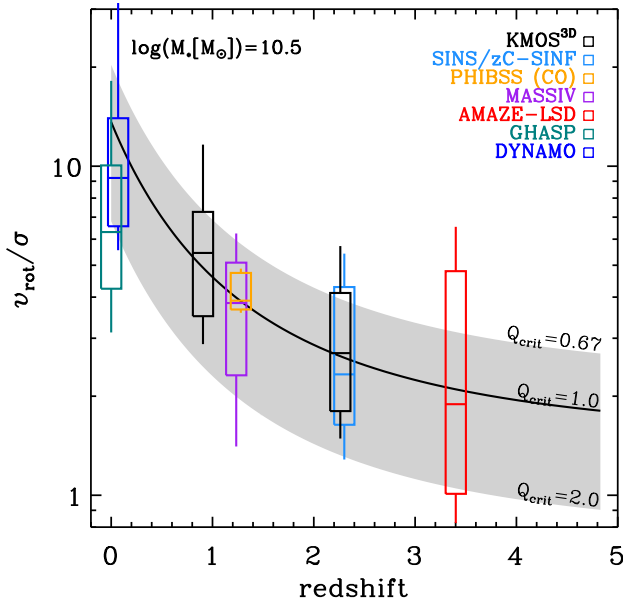


**Figure 11.** Medians (horizontal lines) of the disk stability diagnostic,  $v_{\text{rot}}/\sigma$ , for IFS samples with boxes representing the central 50% of the sample and the vertical lines representing the 90% distribution. The values are adjusted to an average  $\log(M_*) = 10.5$ . The upper and lower boundaries of the curve are the predictions following Equation (8) where  $Q_{\text{crit}} = 0.67, 2.0$  for a thick gas disk and composite disk.  $Q_{\text{crit}} = 1$ , the value adopted in this analysis, is shown by the solid line. The data are from the same surveys as described in Figure 8 and Figure 10.

70% of the detected galaxies resolved. Detections cover  $\gtrsim 3$  dex in SFR and sSFR. Given the depth of the survey, we detect  $[\text{N II}] \lambda 6584$  in 77% of the  $\text{H}\alpha$ -detected galaxies.

First results from the survey reveal that the MS of star formation is dominated by rotating galaxies at both redshift regimes demonstrating the buildup of size, central mass concentration, and ordered rotation when moving to higher galaxy stellar masses. We find 93% of galaxies at  $z \sim 1$  and 74% at  $z \sim 2$  are rotationally supported, as determined from a continuous velocity gradient and  $v_{\text{rot}}/\sigma_0 > 1$ . We find a disk fraction of 58% when applying the additional stricter criteria that the projected velocity dispersion distribution peaks on or near the kinematic center, the velocity gradient is measured along the photometric major axis (for inclined systems), and the closeness of the kinematic centroid to the center of the galaxy continuum. Galaxies well below the MS show rotational signatures while the few galaxies observed so far above the MS are compact with unresolved internal motions. Galaxies that are resolved but not rotating are found primarily at low  $M_*$ . We observe 11 galaxy “close pairs” (within  $500 \text{ km s}^{-1}$  and  $\sim 12 \text{ kpc}$ ) that have a variety of kinematic structure from rotating companions to chaotic motions and are found in all populated regions of the SFR– $M_*$  plane.

With the KMOS<sup>3D</sup> data we confirm a factor of two decrease in ionized gas velocity dispersions from  $50 \text{ km s}^{-1}$  at  $z \sim 2$  and  $25 \text{ km s}^{-1}$  at  $z \sim 1$  using representative populations measured with consistent methods. When these measurements are considered in the context of disk velocity dispersions from  $z = 0$  to 4, we report an evolution of ionized gas velocity

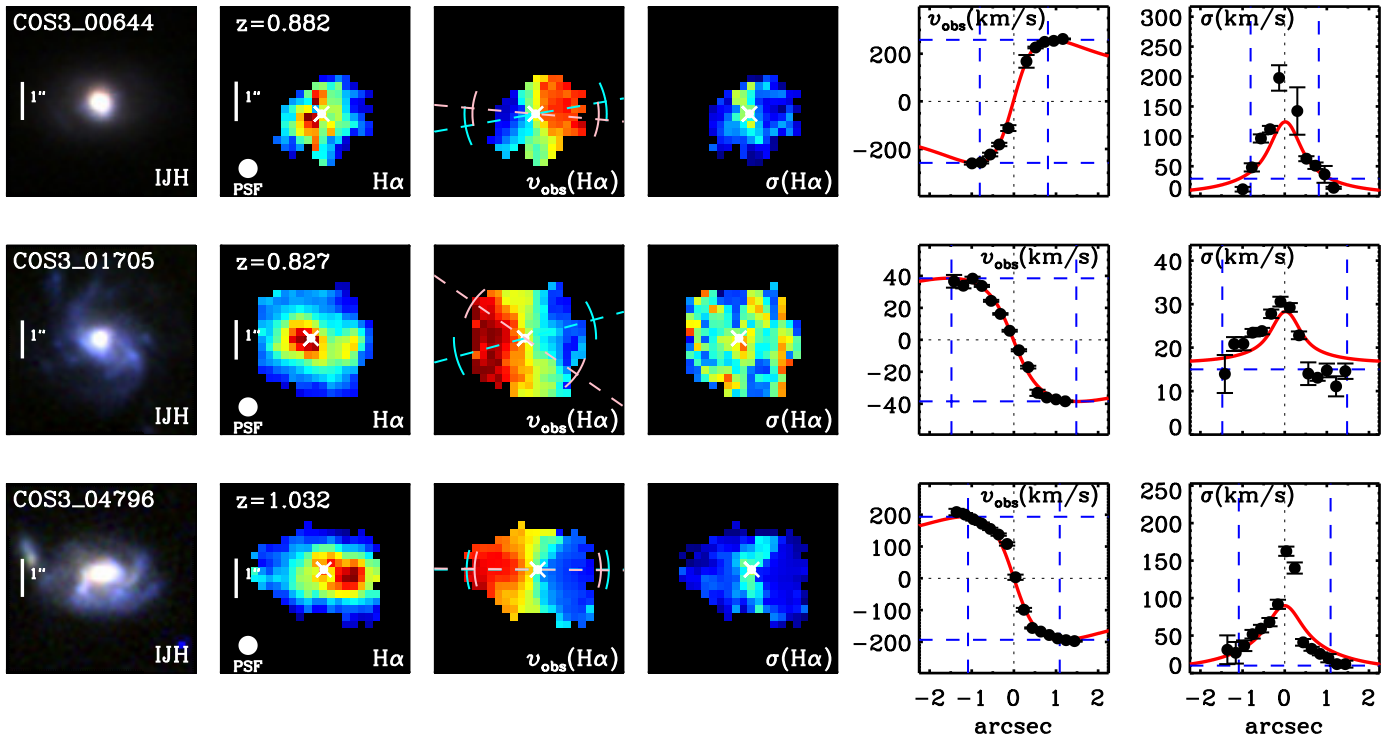


**Figure 12.** *HST* images, kinematic maps and axis profiles for the high-S/N disk galaxies in KMOS<sup>3D</sup> first-year data. From left to right for an individual galaxy: Observed-frame *IJH* color composite image from CANDELS *HST* imaging,  $\text{H}\alpha$  emission map from KMOS, corresponding velocity field, and velocity dispersion field, followed by the velocity and velocity dispersion axis profiles. North is up and east is left for all galaxy images and maps. The axis profiles are extracted along the kinematic PA as denoted by the light blue line over plotted on the velocity map. The photometric PA, as determined by F160W *HST* images, is shown by the pink line. The blue arcs correspond to  $\pm 18^\circ$ , the average misalignment between photometric and kinematic PAs, while the pink arcs correspond to  $\pm 3\sigma$  error on the photometric PA. The white circle in the  $\text{H}\alpha$  image represents the FWHM of the PSF. Exponential disk models fit to the axis profiles, black data points, are shown by the red curves. The velocity fields are scaled by minimum and maximum  $v(r)$  from the corresponding axis profile and velocity dispersion fields are scaled by the minimum pixel dispersion and the maximum dispersion from the dispersion axis profile.

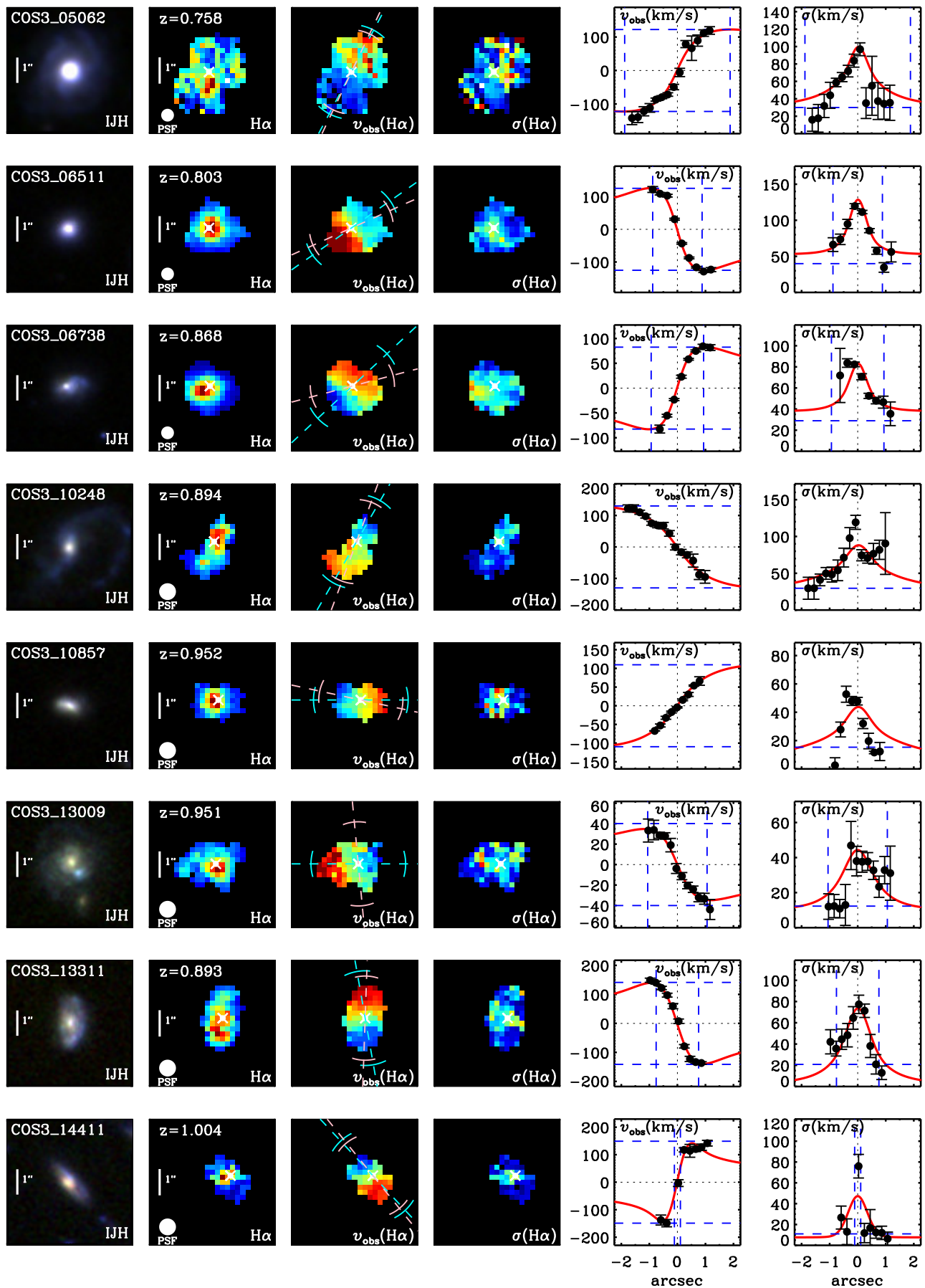


Figure 12. (Continued)

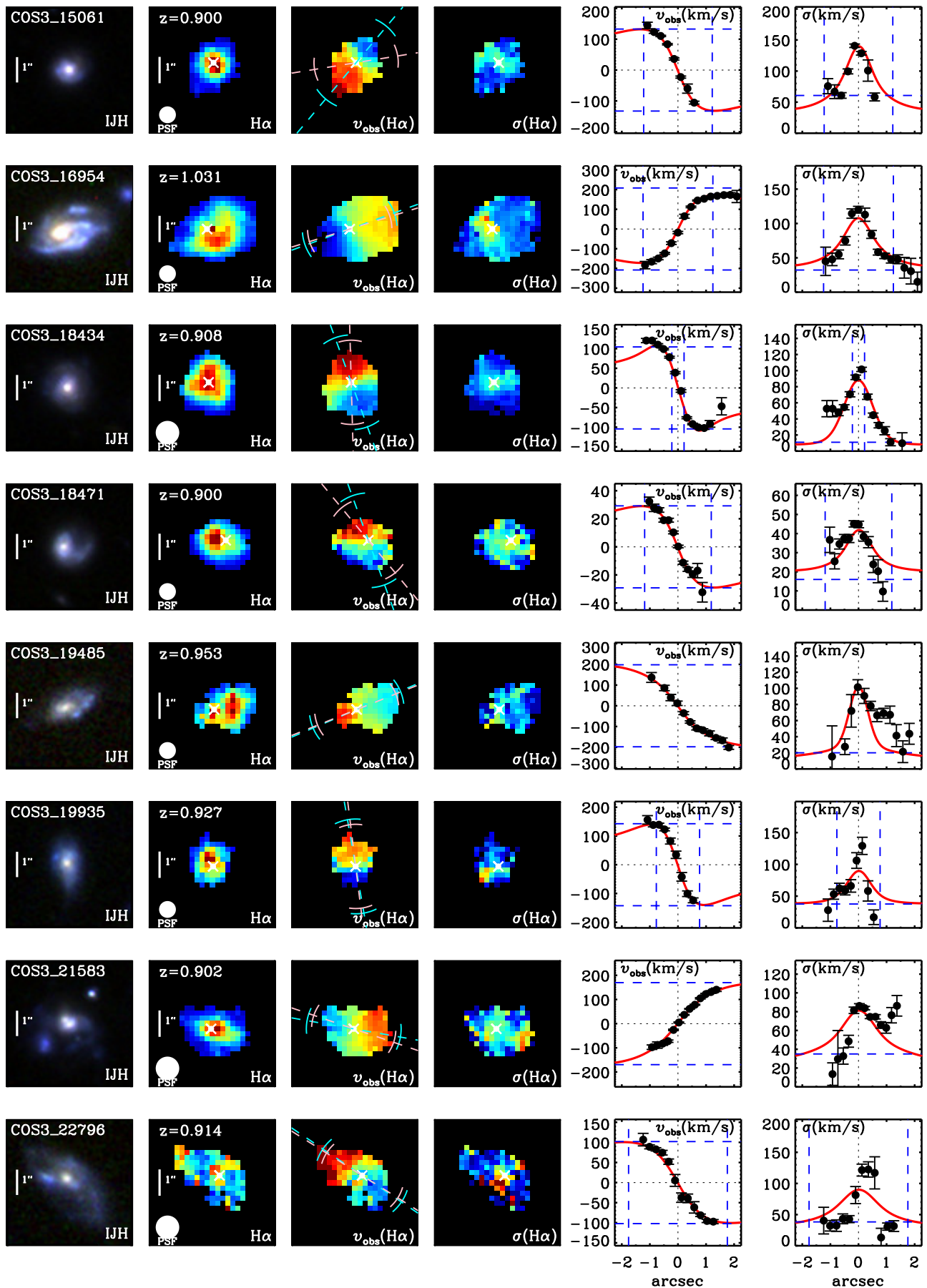


Figure 12. (Continued)

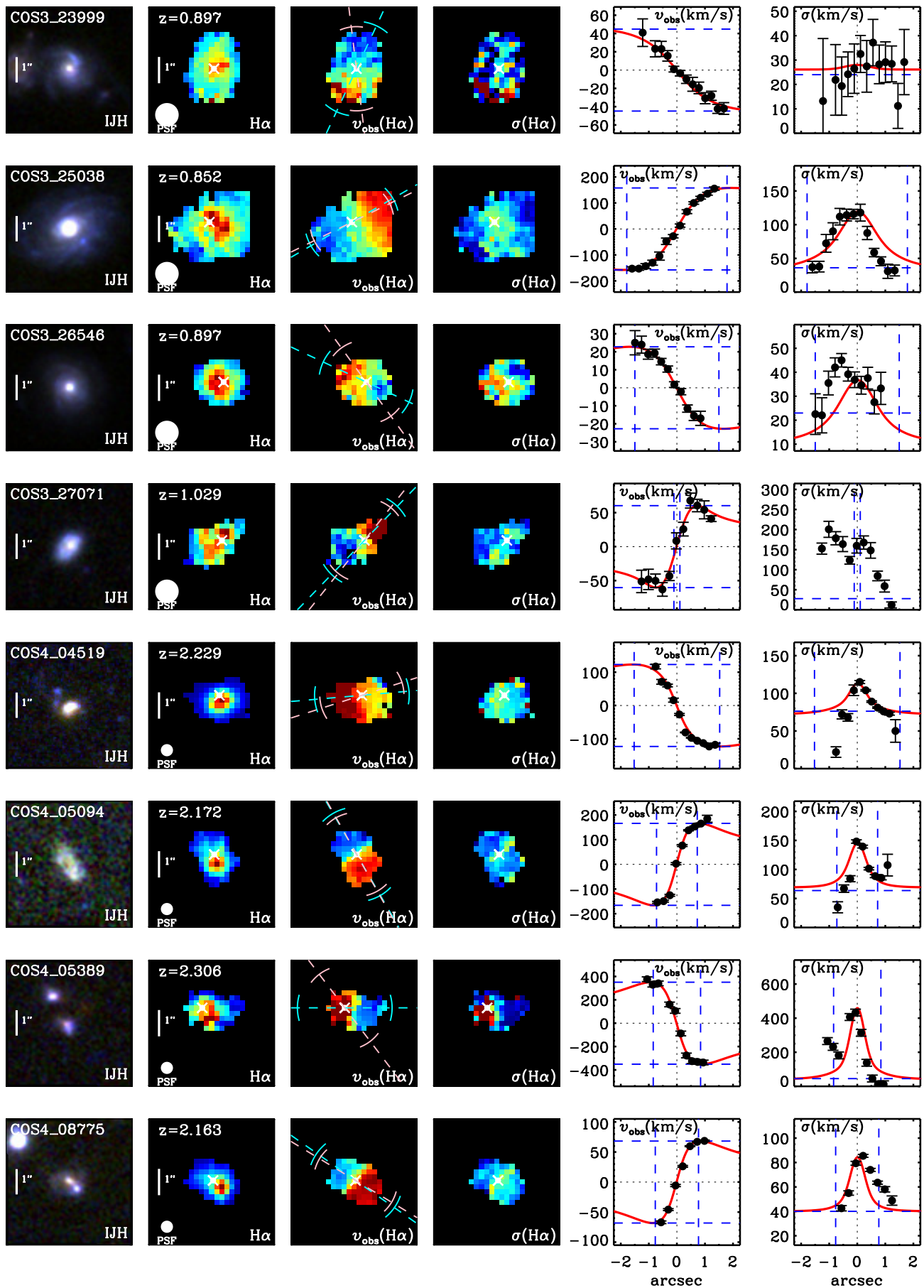


Figure 12. (Continued)

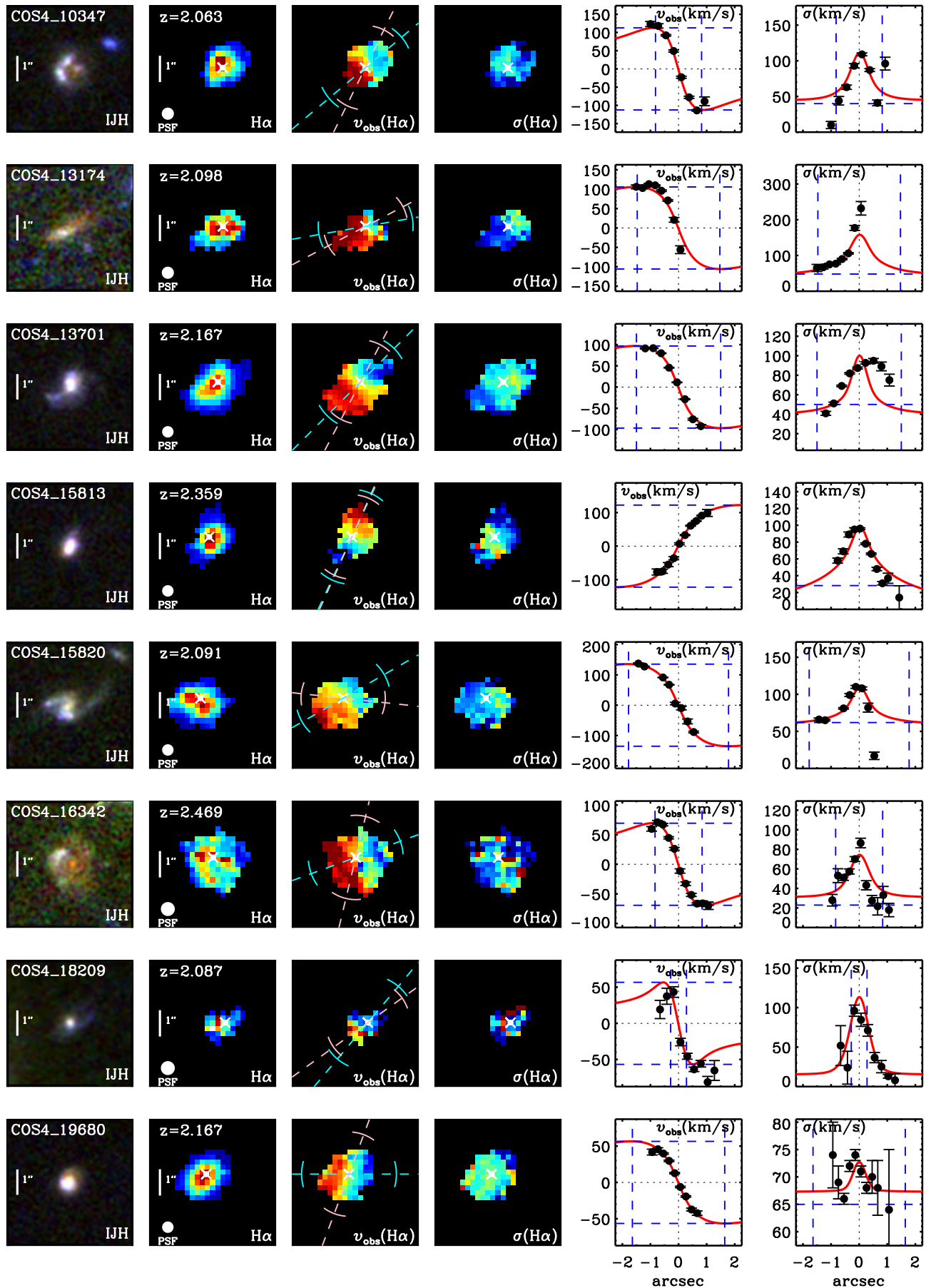


Figure 12. (Continued)

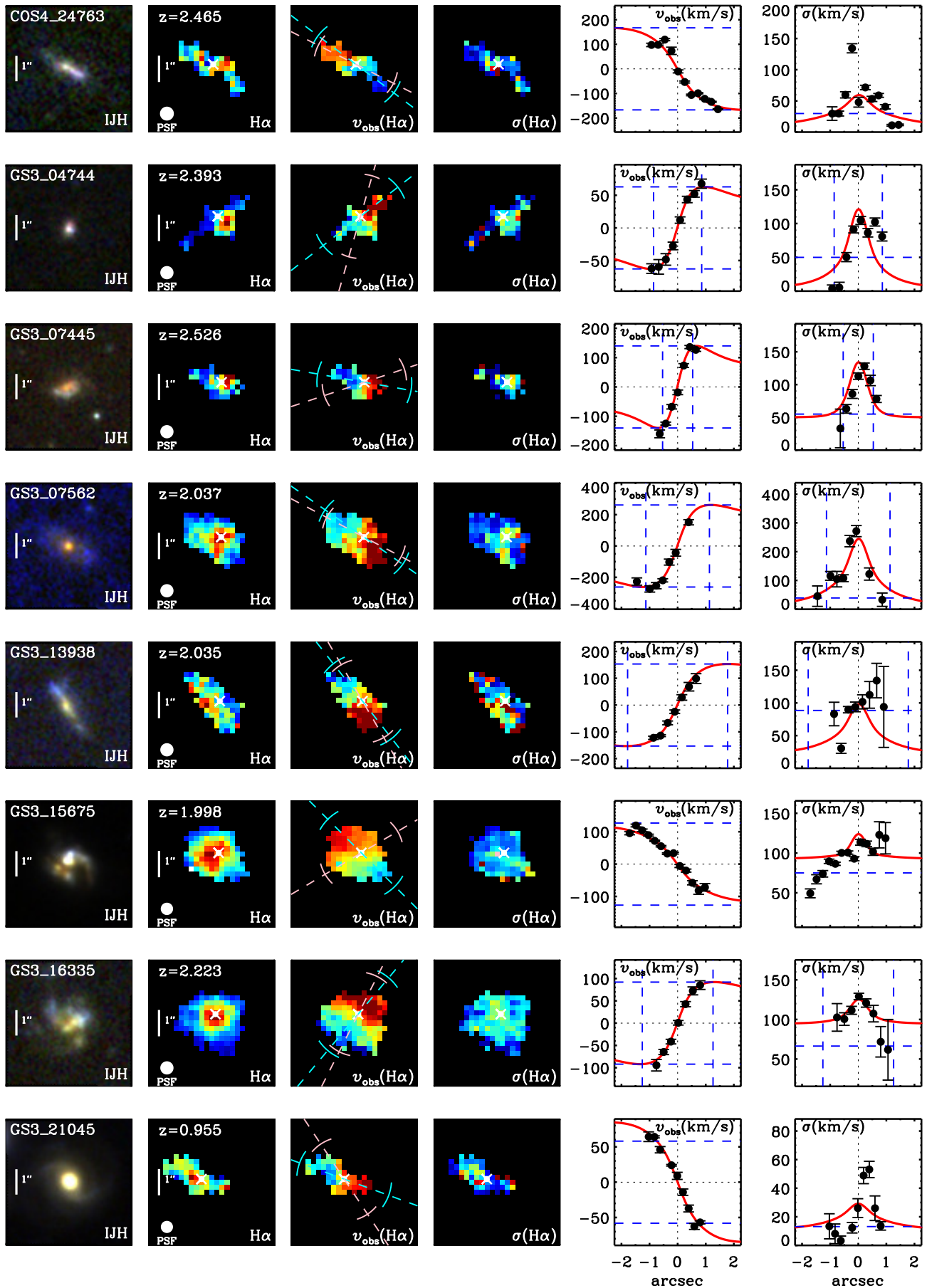


Figure 12. (Continued)

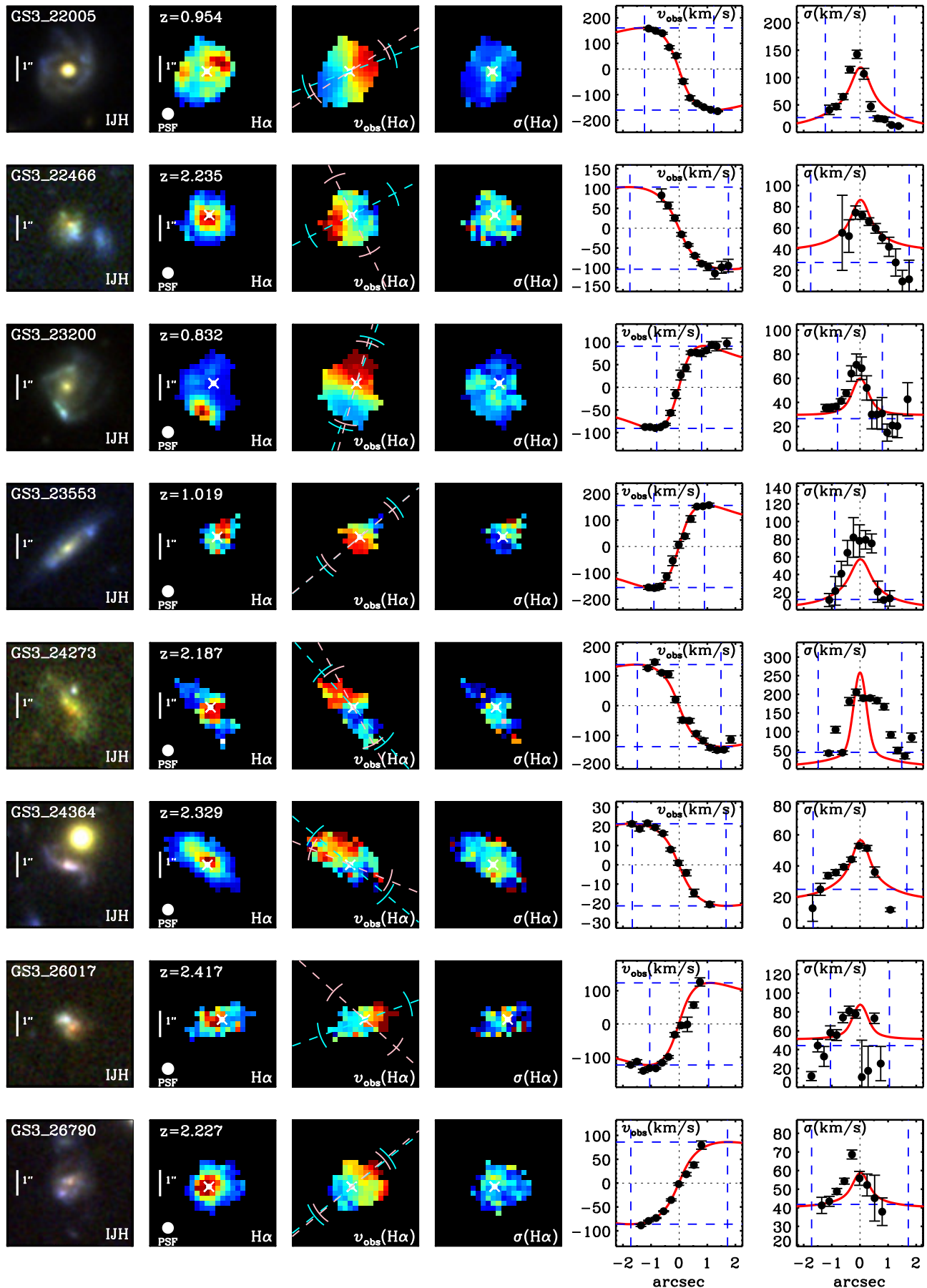


Figure 12. (Continued)

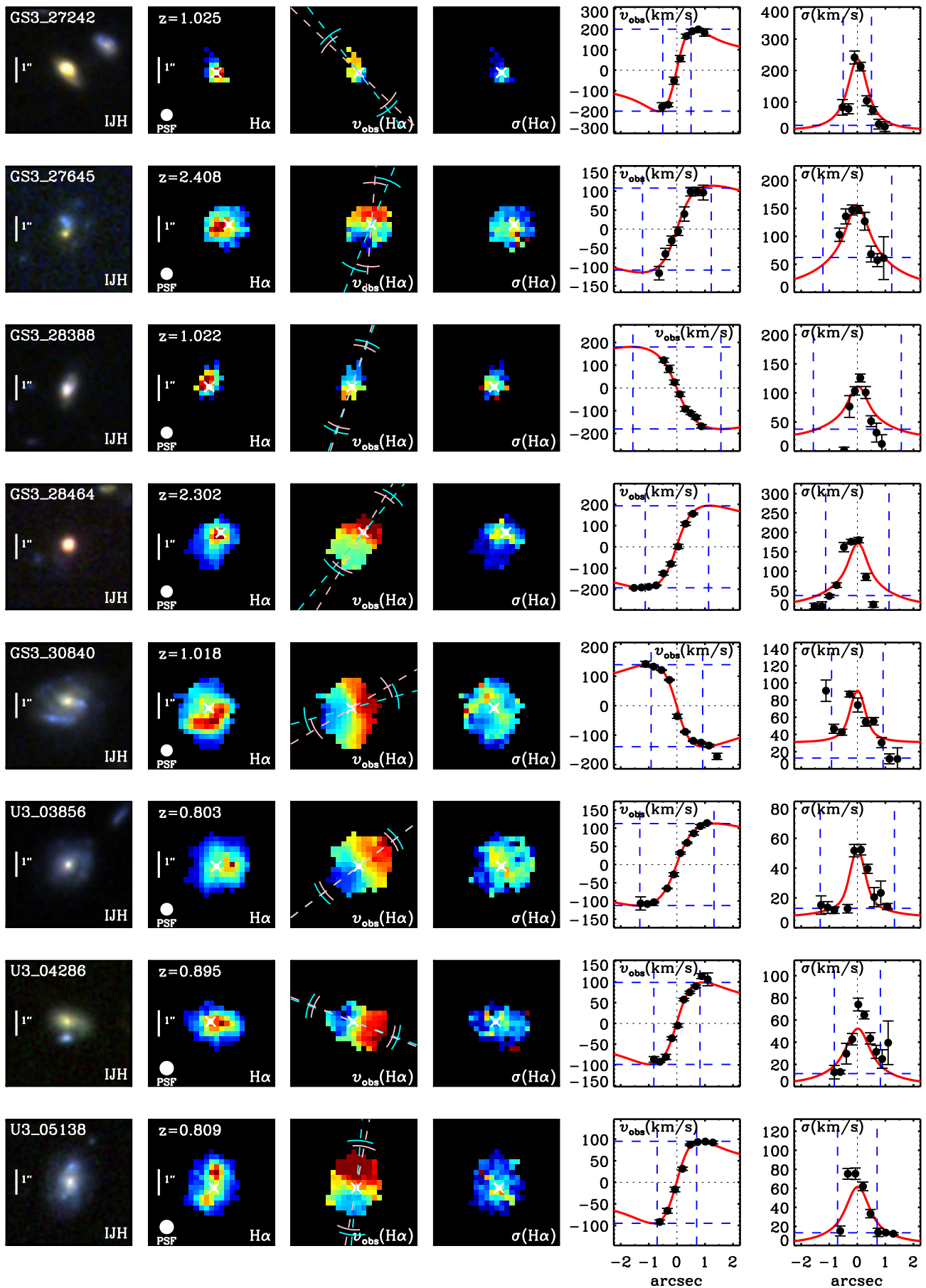


Figure 12. (Continued)

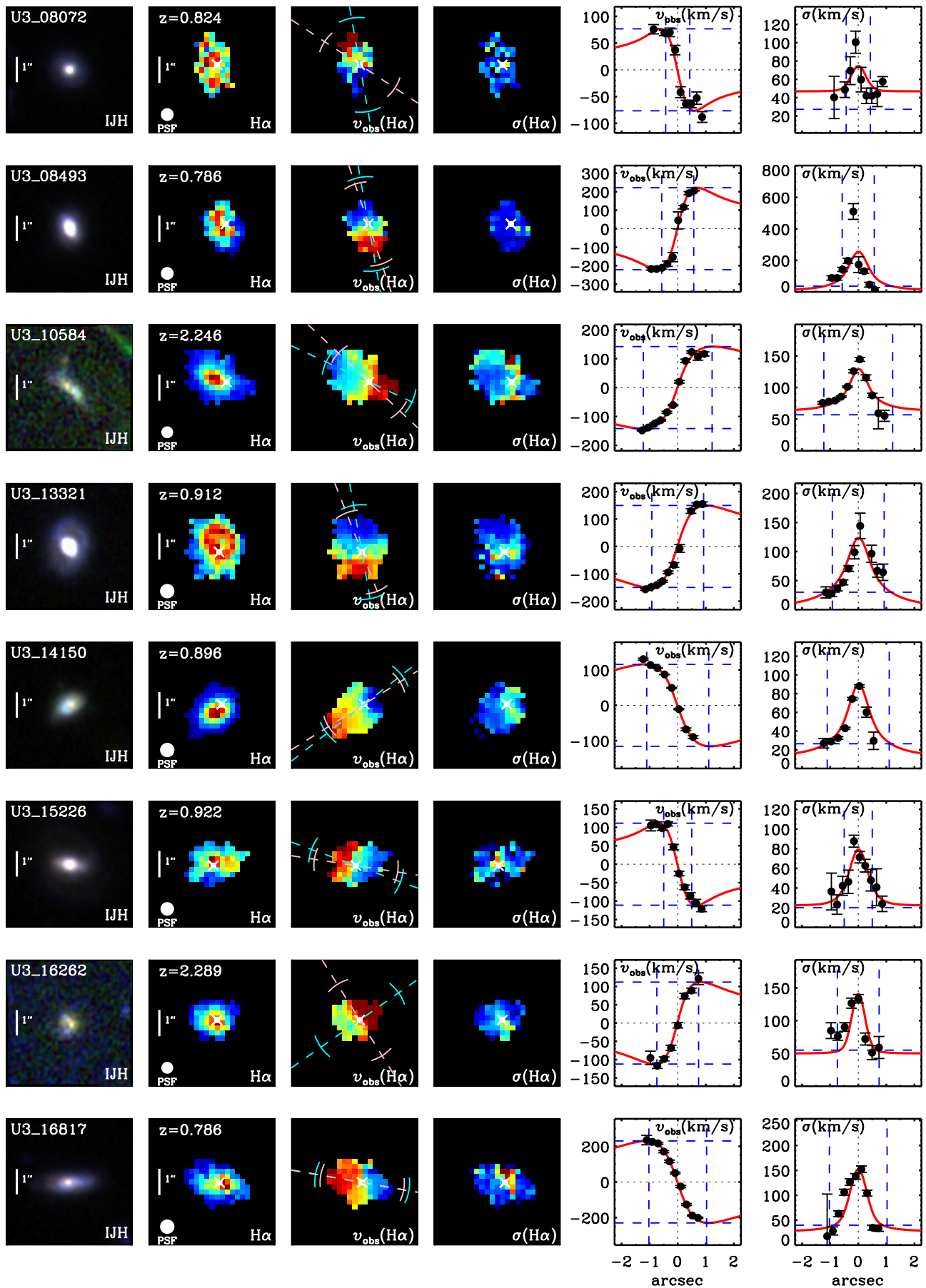


Figure 12. (Continued)

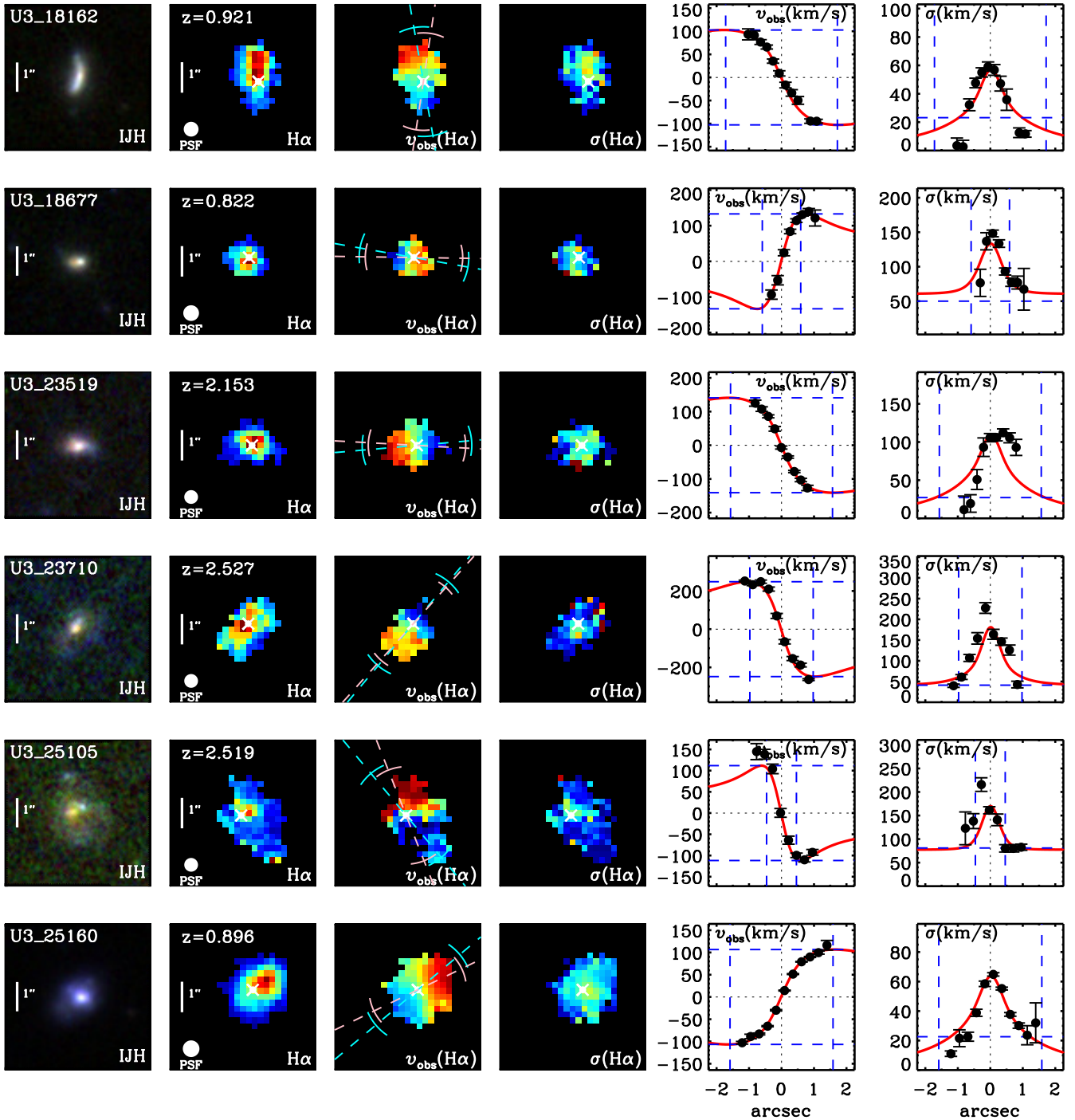


Figure 12. (Continued)

dispersion that closely follows the evolution of specific SFR and gas fractions, consistent with the “equilibrium” or “regulator” model and providing evidence that disk turbulence is being set by the balance of gas fueling and star formation as predicted by marginally stable disk theory.

The new multi-IFU KMOS instrument allows us to take the next major step in IFS surveys of distant galaxies, enabling sensitive observations of large samples across a broad range of redshifts with wider and more uniform coverage of galaxy parameter space. The first-year data and results from our KMOS<sup>3D</sup> survey and other surveys open up new avenues in investigating the early evolution of galaxies. As more data are

collected over the next few years, better constraints on the kinematic and star-forming properties should provide a much more complete picture of the processes driving the growth and star formation shutdown of galaxies at the crucial  $z \sim 0.5\text{--}3$  epochs.

We thank the ESO staff, and in particular the staff at Paranal Observatory, for their helpful and enthusiastic support during the many observing runs over which the KMOS GTO were carried out. We thank the entire KMOS instrument and Commissioning team for their hard work, which allowed our observational program to be carried out so successfully. We also thank the

software development team of SPARK for all their work with us to get the most out of the data. This paper and the KMOS<sup>3D</sup> survey have benefitted from many constructive, insightful, and enthusiastic discussions with many colleagues whom we are very grateful to, especially M. Franx, A. Renzini, K. Whitaker, K. Glazebrook, and R. Bassett. D.J.W. and M.F. acknowledge the support of the Deutsche Forschungsgemeinschaft via Project ID 387/1-1. We thank the referee for a thorough reading and valuable comments.

## APPENDIX

### HIGH-S/N DISK SAMPLE IN FIRST-YEAR DATA

We present the observed-frame *IJH* images, H $\alpha$  emission maps, velocity, and velocity dispersion fields of the high-S/N disk sample at  $z \sim 1$  and  $z \sim 2$  from the first-year KMOS<sup>3D</sup> data (Figure 12). Velocity and velocity dispersion axis profiles extracted along the kinematic axis in apertures equivalent to the PSF are shown for each galaxy. We fit a Freeman exponential disk model to the velocity axis profile, given by

$$v_{\text{obs}}(r) = \frac{r}{r_0} \sqrt{\pi G \Sigma_0 r_0 (I_0 K_0 - I_1 K_1)}, \quad (\text{A1})$$

where  $\Sigma_0$  is the central disk surface density,  $r_0$  is the exponential radius, and  $I_i$  and  $K_i$  are  $i$ th-order modified Bessel functions (Freeman 1970). The maximal velocity of this model is reached at  $\sim 0.88 \sqrt{\pi G \Sigma_0 r_0}$  at a turnover radius of  $\sim 2.15 r_0$ . Additionally, we fit the approximation for the velocity dispersion in a thick disk ( $\sigma_{02}$ ; Genzel et al. 2008; Cresci et al. 2009) to the dispersion profile with a constant level of intrinsic dispersion,  $\sigma_{01}$ , added in quadrature as described by

$$\sigma_{02}(r) = \frac{v_{\text{rot}}(r) h_z}{r}, \quad (\text{A2})$$

$$\sigma_{\text{mod}}(r) = \sqrt{\sigma_{01}^2 + \sigma_{02}(r)^2}. \quad (\text{A3})$$

The models are convolved with the average PSF of the pointing prior to fitting. In practice for this model, the constant scale height,  $h_z$ , determines the normalization of the  $v_{\text{rot}}/r$  curve in the  $\sigma_{02}$  term while  $\sigma_{01}$  determines the value that the model flattens to at radii beyond the turnover radius. In the cases where  $\sigma_{01} > 0$  the measured velocity dispersion  $\sigma_0$  is  $\sigma_0 \approx \sigma_{01}$ . When  $\sigma_{01}$  is equal to zero,  $\sigma_{\text{mod}}$  approaches zero at infinity.

## REFERENCES

Arribas, S., Colina, L., Bellocchi, E., Maiolino, R., & Villar-Martín, M. 2014, *A&A*, 568, A14

Aumer, M., Burkert, A., Johansson, P. H., & Genzel, R. 2010, *ApJ*, 719, 1230

Bassett, R., Glazebrook, K., Fisher, D. B., et al. 2014, *MNRAS*, 442, 3206

Bigiel, F., Leroy, A. K., Walter, F., et al. 2011, *ApJL*, 730, L13

Bluck, A. F. L., Conselice, C. J., Bouwens, R. J., et al. 2009, *MNRAS*, 394, L51

Bongiorno, A., Merloni, A., Brusa, M., et al. 2012, *MNRAS*, 427, 3103

Bouché, N., Dekel, A., Genzel, R., et al. 2010, *ApJ*, 718, 1001

Bournaud, F., Chapon, D., Teyssier, R., et al. 2011, *ApJ*, 730, 4

Bournaud, F., Elmegreen, B. G., Teyssier, R., Block, D. L., & Puerari, I. 2010, *MNRAS*, 409, 1088

Bouwens, R. J., Illingworth, G. D., Oesch, P. A., et al. 2012, *ApJ*, 754, 83

Bower, R. G., Benson, A. J., Malbon, R., et al. 2006, *MNRAS*, 370, 645

Brammer, G., van Dokkum, P., Franx, M., et al. 2012, *ApJS*, 200, 13

Brusa, M., Fiore, F., Santini, P., et al. 2009, *A&A*, 507, 1277

Cacciato, M., Dekel, A., & Genel, S. 2012, *MNRAS*, 421, 818

Calzetti, D., Armus, L., Bohlin, R. C., et al. 2000, *ApJ*, 533, 682

Chabrier, G. 2003, *PASP*, 115, 763

Civano, F., Elvis, M., Brusa, M., et al. 2012, *ApJS*, 201, 30

Combes, F., García-Burillo, S., Braine, J., et al. 2011, *A&A*, 528, A124

Contini, T., Garilli, B., Le Fèvre, O., et al. 2012, *A&A*, 539, A91

Cresci, G., Hicks, E. K. S., Genzel, R., et al. 2009, *ApJ*, 697, 115

Daddi, E., Alexander, D. M., Dickinson, M., et al. 2007a, *ApJ*, 670, 173

Daddi, E., Bournaud, F., Walter, F., et al. 2010, *ApJ*, 713, 686

Daddi, E., Dickinson, M., Morrison, G., et al. 2007b, *ApJ*, 670, 156

Damen, M., Labbé, I., Franx, M., et al. 2009, *ApJ*, 690, 937

Davé, R., Finlator, K., & Oppenheimer, B. D. 2012, *MNRAS*, 421, 98

Davies, R., Agudo Berbel, A., Wierorke, E., et al. 2013, *A&A*, 558, A56

Davies, R., Förster Schreiber, N. M., Cresci, G., et al. 2011, *ApJ*, 741, 69

Dekel, A., & Mandelker, N. 2014, *MNRAS*, 444, 2071

Dekel, A., Sari, R., & Ceverino, D. 2009, *ApJ*, 703, 785

Dib, S., Bell, E., & Burkert, A. 2006, *ApJ*, 638, 797

Dutton, A. A., van den Bosch, F. C., & Dekel, A. 2010, *MNRAS*, 405, 1690

Elbaz, D., Daddi, E., Le Borgne, D., et al. 2007, *A&A*, 468, 33

Elbaz, D., Dickinson, M., Hwang, H. S., et al. 2011, *A&A*, 533, A119

Elmegreen, B. G., & Burkert, A. 2010, *ApJ*, 712, 294

Elmegreen, B. G., & Elmegreen, D. M. 2006, *ApJ*, 650, 644

Epinat, B., Amram, P., Balkowski, C., & Marcelin, M. 2010, *MNRAS*, 401, 2113

Epinat, B., Contini, T., Le Fèvre, O., et al. 2009, *A&A*, 504, 789

Epinat, B., Tasca, L., Amram, P., et al. 2012, *A&A*, 539, A92

Erb, D. K., Steidel, C. C., Shapley, A. E., Pettini, M., & Adelberger, K. L. 2004, *ApJ*, 612, 122

Forbes, J., Krumholz, M., & Burkert, A. 2012, *ApJ*, 754, 48

Förster Schreiber, N. M., Genzel, R., Bouché, N., et al. 2009, *ApJ*, 706, 1364

Förster Schreiber, N. M., Genzel, R., Lehnert, M. D., et al. 2006, *ApJ*, 645, 1062

Förster Schreiber, N. M., Genzel, R., Newman, S. F., et al. 2014, *ApJ*, 787, 38

Franx, M., Illingworth, G., & de Zeeuw, T. 1991, *ApJ*, 383, 112

Freeman, K. C. 1970, *ApJ*, 160, 811

Genel, S., Bouché, N., Naab, T., Sternberg, A., & Genzel, R. 2010, *ApJ*, 719, 229

Genzel, R., Burkert, A., Bouché, N., et al. 2008, *ApJ*, 687, 59

Genzel, R., Förster Schreiber, N. M., Lang, P., et al. 2014a, *ApJ*, 785, 75

Genzel, R., Förster Schreiber, N. M., Rosario, D., et al. 2014b, *ApJ*, 796, 7

Genzel, R., Newman, S., Jones, T., et al. 2011, *ApJ*, 733, 101

Genzel, R., Tacconi, L. J., Eisenhauer, F., et al. 2006, *Natur*, 442, 786

Genzel, R., Tacconi, L. J., Lutz, D., et al. 2014c, arXiv:1409.1171

Glazebrook, K. 2013, *PASA*, 30, e056

Gnerucci, A., Marconi, A., Cresci, G., et al. 2011, *A&A*, 528, A88

González, V., Bouwens, R., Illingworth, G., et al. 2014, *ApJ*, 781, 34

Green, A. W., Glazebrook, K., McGregor, P. J., et al. 2010, *Natur*, 467, 684

Green, A. W., Glazebrook, K., McGregor, P. J., et al. 2014, *MNRAS*, 437, 1070

Grogin, N. A., Kocevski, D. D., Faber, S. M., et al. 2011, *ApJS*, 197, 35

Guo, Q., White, S., Li, C., & Boylan-Kolchin, M. 2010, *MNRAS*, 404, 1111

Hainline, K. N., Shapley, A. E., Greene, J. E., et al. 2012, *ApJ*, 760, 74

Harrison, C. M., Alexander, D. M., Swinbank, A. M., et al. 2012, *MNRAS*, 426, 1073

Hopkins, P. F., Bundy, K., Croton, D., et al. 2010, *ApJ*, 715, 202

Hung, C.-L., Sanders, D. B., Casey, C. M., et al. 2013, *ApJ*, 778, 129

Immeli, A., Samland, M., Gerhard, O., & Westera, P. 2004, *A&A*, 413, 547

Kartaltepe, J. S., Dickinson, M., Alexander, D. M., et al. 2012, *ApJ*, 757, 23

Kassin, S. A., Weiner, B. J., Faber, S. M., et al. 2012, *ApJ*, 758, 106

Kim, W.-T., & Ostriker, E. C. 2007, *ApJ*, 660, 1232

Koekemoer, A. M., Faber, S. M., Ferguson, H. C., et al. 2011, *ApJS*, 197, 36

Krajinović, D., Cappellari, M., de Zeeuw, P. T., & Copin, Y. 2006, *MNRAS*, 366, 787

Lackner, C. N., Silverman, J. D., Salvato, M., et al. 2014, *AJ*, 148, 137

Lang, P., Wuyts, S., Somerville, R., et al. 2014, *ApJ*, 788, 11

Law, D. R., Steidel, C. C., Erb, D. K., et al. 2007, *ApJ*, 669, 929

Law, D. R., Steidel, C. C., Erb, D. K., et al. 2009, *ApJ*, 697, 2057

Law, D. R., Steidel, C. C., Shapley, A. E., et al. 2012a, *ApJ*, 745, 85

Law, D. R., Steidel, C. C., Shapley, A. E., et al. 2012b, *ApJ*, 759, 29

Le Fèvre, O., Abraham, R., Lilly, S. J., et al. 2000, *MNRAS*, 311, 565

Leroy, A. K., Walter, F., Bigiel, F., et al. 2009, *AJ*, 137, 4670

Leroy, A. K., Walter, F., Brinks, E., et al. 2008, *AJ*, 136, 2782

Lilly, S. J., Carollo, C. M., Pipino, A., Renzini, A., & Peng, Y. 2013, *ApJ*, 772, 119

Lotz, J. M., Davis, M., Faber, S. M., et al. 2008, *ApJ*, 672, 177

Lutz, D., Poglitsch, A., Altieri, B., et al. 2011, *A&A*, 532, A90

Magnelli, B., Popesso, P., Berta, S., et al. 2013, *A&A*, 553, A132

Martig, M., Bournaud, F., Teyssier, R., & Dekel, A. 2009, *ApJ*, 707, 250

Mullaney, J. R., Daddi, E., Béthermin, M., et al. 2012, *ApJL*, 753, L30

Nelson, E. J., van Dokkum, P. G., Momcheva, I., et al. 2013, *ApJL*, 763, L16

Nestor, D. B., Johnson, B. D., Wild, V., et al. 2011, *MNRAS*, 412, 1559

- Nesvadba, N. P. H., Lehnert, M. D., De Breuck, C., Gilbert, A. M., & van Breugel, W. 2008, *A&A*, **491**, 407
- Newman, S. F., Genzel, R., Förster Schreiber, N. M., et al. 2013, *ApJ*, **767**, 104
- Newman, S. F., Shapiro Griffin, K., Genzel, R., et al. 2012, *ApJ*, **752**, 111
- Noeske, K. G., Weiner, B. J., Faber, S. M., et al. 2007, *ApJL*, **660**, L43
- Peng, Y.-j., Lilly, S. J., Kovač, K., et al. 2010, *ApJ*, **721**, 193
- Powell, L. C., Bournaud, F., Chapon, D., & Teyssier, R. 2013, *MNRAS*, **434**, 1028
- Reddy, N. A., Erb, D. K., Steidel, C. C., et al. 2005, *ApJ*, **633**, 748
- Reshetnikov, V. P., Dettmar, R.-J., & Combes, F. 2003, *A&A*, **399**, 879
- Rodighiero, G., Daddi, E., Baronchelli, I., et al. 2011, *ApJL*, **739**, L40
- Rosario, D. J., Santini, P., Lutz, D., et al. 2012, *A&A*, **545**, A45
- Saintonge, A., Kauffmann, G., Wang, J., et al. 2011, *MNRAS*, **415**, 61
- Saintonge, A., Lutz, D., Genzel, R., et al. 2013, *ApJ*, **778**, 2
- Saintonge, A., Tacconi, L. J., Fabello, S., et al. 2012, *ApJ*, **758**, 73
- Schaye, J., Crain, R. A., Bower, R. G., et al. 2015, *MNRAS*, **446**, 521
- Schmidt, K. B., Rix, H.-W., da Cunha, E., et al. 2013, *MNRAS*, **432**, 285
- Shapiro, K. L., Genzel, R., Förster Schreiber, N. M., et al. 2008, *ApJ*, **682**, 231
- Shapiro, K. L., Genzel, R., Quataert, E., et al. 2009, *ApJ*, **701**, 955
- Sharples, R., Bender, R., Agudo Berbel, A., et al. 2013, *Msngr*, **151**, 21
- Sharples, R. M., Bender, R., Lehnert, M. D., et al. 2004, *Proc. SPIE*, **5492**, 1179
- Skelton, R. E., Whitaker, K. E., Momcheva, I. G., et al. 2014, *ApJS*, **214**, 24
- Sobral, D., Swinbank, A. M., Stott, J. P., et al. 2013, *ApJ*, **779**, 139
- Sparre, M., Hayward, C. C., Springel, V., et al. 2014, arXiv:1409.0009
- Stark, D. P., Schenker, M. A., Ellis, R., et al. 2013, *ApJ*, **763**, 129
- Steidel, C. C., Erb, D. K., Shapley, A. E., et al. 2010, *ApJ*, **717**, 289
- Stott, J. P., Sobral, D., Smail, I., et al. 2013, *MNRAS*, **430**, 1158
- Stott, J. P., Sobral, D., Swinbank, A. M., et al. 2014, *MNRAS*, **443**, 2695
- Swinbank, A. M., Smail, I., Sobral, D., et al. 2012, *ApJ*, **760**, 130
- Tacchella, S., Lang, P., Carollo, C. M., et al. 2014, *ApJ*, submitted (arXiv:1411.7034)
- Tacconi, L. J., Genzel, R., Neri, R., et al. 2010, *Natur*, **463**, 781
- Tacconi, L. J., Neri, R., Genzel, R., et al. 2013, *ApJ*, **768**, 74
- Toomre, A. 1964, *ApJ*, **139**, 1217
- Ueda, Y., Watson, M. G., Stewart, I. M., et al. 2008, *ApJS*, **179**, 124
- van der Kruit, P. C., & Allen, R. J. 1978, *ARA&A*, **16**, 103
- van der Wel, A., Bell, E. F., Häussler, B., et al. 2012, *ApJS*, **203**, 24
- van der Wel, A., Chang, Y.-Y., Bell, E. F., et al. 2014a, *ApJL*, **792**, L6
- van der Wel, A., Franx, M., van Dokkum, P. G., et al. 2014b, *ApJ*, **788**, 28
- Vergani, D., Epinat, B., Contini, T., et al. 2012, *A&A*, **546**, A118
- Vogelsberger, M., Genel, S., Sijacki, D., et al. 2013, *MNRAS*, **436**, 3031
- Wegner, M., & Muschelok, B. 2008, *Proc. SPIE*, **7019**, 70190T
- Weiner, B. J., Coil, A. L., Prochaska, J. X., et al. 2009, *ApJ*, **692**, 187
- Weiner, B. J., Willmer, C. N. A., Faber, S. M., et al. 2006, *ApJ*, **653**, 1027
- Whitaker, K. E., Franx, M., Leja, J., et al. 2014, *ApJ*, **795**, 104
- Whitaker, K. E., Kriek, M., van Dokkum, P. G., et al. 2012a, *ApJ*, **745**, 179
- Whitaker, K. E., van Dokkum, P. G., Brammer, G., & Franx, M. 2012b, *ApJL*, **754**, L29
- Whitaker, K. E., van Dokkum, P. G., Brammer, G., et al. 2013, *ApJL*, **770**, L39
- Wisnioski, E., Glazebrook, K., Blake, C., et al. 2011, *MNRAS*, **417**, 2601
- Wright, S. A., Larkin, J. E., Law, D. R., et al. 2009, *ApJ*, **699**, 421
- Wuyts, S., Förster Schreiber, N. M., Genzel, R., et al. 2012, *ApJ*, **753**, 114
- Wuyts, S., Förster Schreiber, N. M., Lutz, D., et al. 2011a, *ApJ*, **738**, 106
- Wuyts, S., Förster Schreiber, N. M., Nelson, E. J., et al. 2013, *ApJ*, **779**, 135
- Wuyts, S., Förster Schreiber, N. M., van der Wel, A., et al. 2011b, *ApJ*, **742**, 96
- Wuyts, E., Kurk, J., Förster Schreiber, N. M., et al. 2014, *ApJL*, **789**, L40
- Xue, Y. Q., Luo, B., Brandt, W. N., et al. 2011, *ApJS*, **195**, 10